Ultra-Wideband Radar for Robust Inspection Drone in Underground Coal Mines

by

Fernando Fleury Pereira Cunha

Submitted to the Department of Mechanical Engineering
in partial fulfillment of the requirements for the degree of

Master of Science in Mechanical Engineering

at the

MASSACHUSETTS INSTITUTE OF TECHNOLOGY

September 2017

Signature redacted

Author .....
Department of Mechanical Engineering
August 10th, 2017

Certified by..... Signature redacted .....
Kamal Youcef-Toumi
Professor
Thesis Supervisor

Accepted by ..... Signature redacted .....
Rohan Abeyaratne
Chairman, Department Committee on Graduate Theses

Ultra-Wideband Radar for Robust Inspection Drone in Underground Coal Mines

by

Fernando Fleury Pereira Cunha

Submitted to the Department of Mechanical Engineering
on August 10th, 2017, in partial fulfillment of the
requirements for the degree of
Master of Science in Mechanical Engineering

Abstract

Coal mines pose a high safety risk for human workers. An autonomous inspection drone would enable a coal mine operation to reduce this risk by minimizing the time spent by workers inside the mine. This inspection drone must be highly robust to the harsh environment of an underground coal mine, with high levels of coal dust and humidity that can obstruct many conventional sensing methods. For high functionality, the drone must sense and avoid potential obstacles and as well as inspect and map the mining wall face. The objective of this paper is to present ultra-wideband (UWB) radar as a robust sensing solution to this challenging environment and validate its performance in the typical coal mine environment, both statically and dynamically.

Thesis Supervisor: Kamal Youcef-Toumi
Title: Professor

Acknowledgments

I would like to thank my advisor, Professor Kamal Youcef-Toumi, for his guidance on this project. His advice and help were invaluable to the success of this thesis. Further, he was always approachable and friendly, making it easy to ask for guidance when it was needed. Working with Kamal has undoubtedly made me a stronger researcher.

I am also incredibly grateful to my lab colleagues who worked with me and supported me on this project. Bo Jiang, Luke Roberto, Zachary Zumbo, Shuanwei Cui, and Yongxiang Xu were instrumental to the success of this study. This project was truly a collaborative effort, and they all contributed to the success of this study.

I would also like to acknowledge the Beijing Tiandi-Marco Electro-Hydraulic Control System Company Ltd, in Beijing, China. Their generosity made this project possible, and I am grateful for their support.

Finally, I would like to thank my family, who have always guided me and been a constant source of support through this project and many others. They gave me the strength and motivation I needed to successfully complete this study.

Contents

List of Figures

List of Tables

Chapter 1

Introduction

1.1 Motivation for Autonomous Drone in Coal Mines

Coal mining poses many risks for human workers, many of which often prove fatal. Though coal mining is a relatively safe practice in the United States with 8 recorded deaths in 2016 [1], the first ever recorded year with fewer than 10 deaths, in 2010 there were over 2000 recorded coal mining deaths caused by accidents in China [2]. These deaths are caused primarily by ceiling collapse and gas related accidents, the two most deadly types of accidents [2]. Figure 1-1 demonstrates the number of deaths caused by accidents in Chinese coal mines over the years 1993 to 2010.

A significant number of coal miners also perish each year due to heath issues unrelated to mining accidents. Over 6000 coal miners perish each year in China from pneumoconiosis, commonly referred to as "black lung disease." This disease is caused by inhalation of dust into the lungs over long periods of time, indicating that coal miners face serious long-term health concerns as well [3]. Although the number of fatalities is slowly declining each year, these numbers are still unacceptably high.

A primary reason for the large number of coal related deaths in China is the large amount of coal produced. From 1992 until 2010 China produced over 1 billion tons of coal each year, making up over 70% of China's energy use [2]. China has limited petroleum resources, and coal energy has been paramount to the economic development of China over the past 60 years [2]. For these reasons, coal use has only

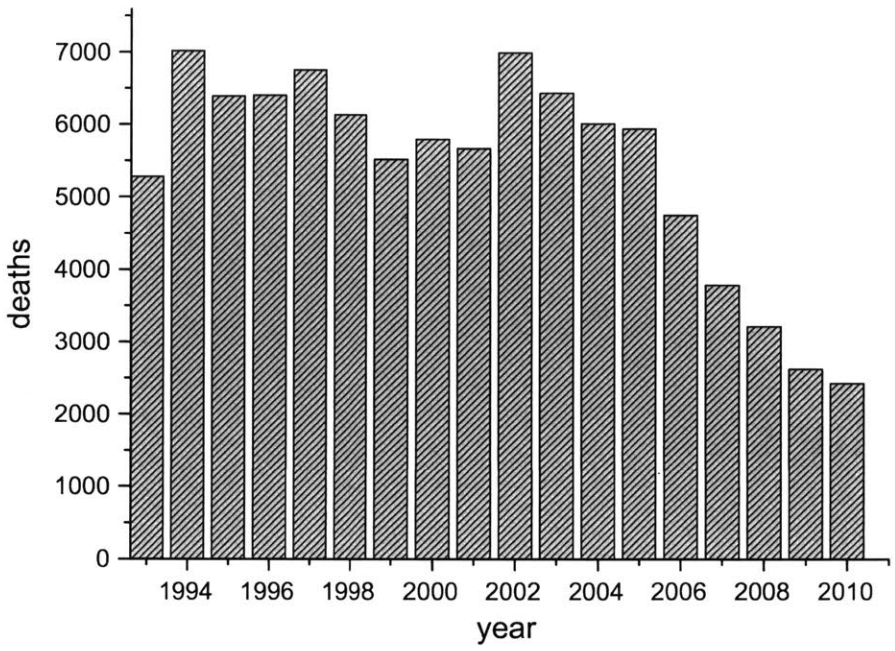

Figure 1-1: Deaths in China's coal mines caused by by accidents, 1993-2010 [2]

grown in China, and coal mine related accidents and deaths remain a serious issue in this industry.

To reduce this loss of life, automation is being explored in the mining industry. The goal of this automation is to remove human workers from the mining wall face, to mitigate the risk associated with coal mining. The autonomous, or semi-autonomous, mining equipment could then be supervised and operated from a safe base station, without any airborne coal dust, risk of mining accidents, or machinery operating nearby. This would ensure the safety of the of the human workers without affecting the production of the mine.

This study explores in particular an autonomous inspection drone. The purpose of this inspection drone would be to stream high definition video to a worker in a safe location, allowing this worker to observe the mining equipment and ensure normal operation from afar. This would allow inspection of the heavy mining machinery without any risk to the safety of the human worker.

In order to navigate successfully, any autonomous equipment must be capable of detecting obstacles and avoiding them, including the inspection drone described

above. Obstacle detection is a key factor in autonomous navigation, and will be the principal focus of this study. Any partially or completely autonomous vehicle must be able to sense its surroundings, determine if an obstacle bars its path, and select a new path that avoids this obstacle. This is the first step in autonomy, and requires a reliable sensor to detect any potential obstacles. In the particular case of a coal mine, this sensor must also be robust to the adverse conditions present.

This study analyzes different sensor options, selects an appropriate sensor for obstacle detection in a coal mine environment, and then validates experimentally that this sensor is robust to the expected conditions in a coal mine.

1.1.1 Challenges for Obstacle Detection

The coal mine environment poses many challenges for obstacle detection and navigation. The primary challenge is the high concentrations of coal dust that may obscure the view of the sensors. The sponsoring company of this study, the Beijing Tiandi-Marco Electro-Hydraulic Control System Company Ltd, has given 1 mg/m^3 as the typical airborne coal dust concentration in a coal mine, with a peak level at approximately 4 mg/m^3, though these levels may vary based on the type of mine and any measures taken to reduce dust levels. These were used as baseline values for the tests performed in future chapters. Figure 1-2 illustrates the dusty conditions common in coal mines, as well as showing a longwall shearer, a device used to grind into the wall of a coal mine, with many water sprayers attached for dust mitigation [4].

Another potential challenge is the high humidity. To reduce the amount of airborne dust, water is constantly sprayed onto the wall face, resulting in high levels of moisture present in the air. The typical humidity level, also provided by the sponsor company, is approximately 95% relative humidity, reaching up to 100% in peak conditions. These values will again vary as different mines may employ varying techniques of dust mitigation.

These two conditions present the most challenging adverse conditions when navigating through a coal mine environment. As a result, these were selected as the primary adverse conditions to be tested in this study. This thesis analyzes the ef-

Figure 1-2: A longwall shearer with water sprayers [4]

fects of high coal dust concentrations and high relative humidity levels on sensor performance.

1.2 Common Sensing Methods

Several sensing technologies are commonly used in existing drones, both in industry and research. DJI, a leading commercial drone manufacturer, uses stereo vision, ultrasonic sensors, and dual redundant IMUs in their drones [5]. A new model of theirs, the Phantom 4 Pro pictured in Figure 1-3, is also the first to include infrared sensing as well [5]. This model includes two stereo vision cameras facing forwards, two facing backwards, and two facing downwards, as well as two downward facing ultrasonic sensors and an infrared sensor on each side, allowing it to sense obstacles in five directions, all four sides and downward.

Various studies have explored ultrasonic sensors, commonly used as the most popular, low-cost sensor for obstacle detection [6, 7, 8, 9, 10], while infrared sensors, stereo cameras, and laser range finders (LRFs) are also typical sensors used frequently

Figure 1-3: The DJI Phantom 4 Pro commercial drone [5]

in obstacle detection studies [6, 8, 9, 10, 11, 12]. All studies explored in this text focus on the use of obstacle detection in GPS-denied environments, as no GPS will be available in an underground coal mine.

Ultrasonic (US) sensors are commonly used for obstacle detection. Their simplicity and low cost make these attractive for many applications. These sensors detect obstacles by emitting high frequency sound waves, receiving reflected sound waves, and then using time-of-flight to determine the distance to the obstacle. They are the only common sensing method described that are not based on electromagnetic (EM) waves, relying instead on mechanical sound waves. US is an established sensing method that has existed and been developed for decades, resulting in low-cost, readily available sensors with a variety of options to select from. Most US sensors return an analog voltage proportional to the distance of the nearest detected object. However, despite these benefits, US sensors struggle to detect sound absorbing materials like clothing, typically have low accuracy, and have shorter range than most other detection methods [6, 9].

Infrared (IR) sensors are also commonly explored as fairly low-cost obstacle detection sensors. IR sensors detect emitted infrared waves; all objects above absolute zero

radiate some energy as infrared waves, and the hotter the object the more energy is emitted. Infrared sensors detect these emissions and are commonly thought of as heat sensors, as warmer objects are easier to detect. As a result, IR sensors are capable of detecting people well, but have less resolution than laser range finders and stereo cameras [6, 11]. IR sensors are more robust than other optical sensors in that they can easily see through fog or smoke, and work equally well day or night, but they struggle to see through dust and are easily distorted by flames or other powerful heat sources [11]. When detecting people or for use in foggy environments, IR remains a reliable, capable option, but in clear environments there are better options.

Stereo cameras are a typical choice for use in obstacle detection as well. These sensors can detect optical wavelengths in the visible spectrum, essentially meaning they match what our eyesight is capable of seeing. A stereo camera has two or more lenses allowing it to create a 3D image, similar to how we process images from both our eyes to allow us to see in three dimensions. Stereo cameras are capable of high resolution and accuracy, provided the environment remains clear. This strong performance in conducive environments will immediately drop in any smoke, fog, or dust, for the same reasons we cannot see through fog or dust; optical wavelengths of light do not penetrate these conditions well.

Stereo cameras are also commonly used with simultaneous localization and mapping (SLAM) algorithms, which compile the images taken over time to develop a map of the sensor's surroundings as well as locate itself in this map. Though this is a reliable and effective method of obstacle avoidance and navigation, it is computationally expensive [12, 9]. In fact, the SLAM algorithms are often performed off-board, requiring connection to a separate computer used to perform the more complex tasks [12].

Laser range finders (LRFs) are a more expensive but commonly used sensor as well. LRFs emit a laser beam in the visible spectrum, receive a reflected wave, and then use time-of-flight to determine the distance to the target. This is the exact same principle as US sensors, but with optical wavelengths of light. Many studies suggest that LRFs are the next step in obstacle detection technology, due to their simplicity,

high accuracy, and long range [9, 10, 12]. They do not require complex algorithms and can simply output the distance to the nearest obstacle. However, as with stereo cameras, they are based on optical wavelengths and are unsuitable in conditions of smoke, fog, dust, or other adverse conditions. Some studies have analyzed LRFs in detail to gauge their performance in these adverse conditions, finding them unusuable [13, 14].

Ultrasonic sensors were the only sensors discussed that are robust to the conditions present in a coal mine. However, due to its low accuracy, relatively short range, and inability to detect clothing or soft materials, it was not selected for further testing. As there may be workers present in the coal mine while the inspection drone is operating, it must be able to detect and avoid collisions with these workers. After testing an unmanned ground vehicle combining a ring of US sensors and LRFs, [9] found that though functional in smoky conditions, the US sensors were markedly less accurate and noisy when operating on their own.

In the literature review above, ultra-wideband (UWB) radar was also presented as an alternative to US [9]. UWB radar, an overlooked sensor method that has grown in popularity recently, provides similarly robust performance, but with stronger accuracy capabilities [9]. This technology was explored and ultimately selected as the best option for obstacle detection in an underground coal mine.

1.2.1 Ultra-Wideband Radar

Ultra-wideband radar is an emerging technology that functions in a similar method to US and LRF sensors. Like these two, radar utilizes time-of-flight to characterize the distance to a measured target. Like LRFs, radar utilizes electromagnetic waves, as opposed to sound waves used by US. However, unlike LRFs, radar utilizes radio waves as opposed to waves in the visible light spectrum. These radio waves have much longer wavelengths than visible or infrared light, giving them different propagating characteristics. In this case, this is beneficial, as radio waves are much more capable of penetrating dust and smoke than visible light waves. UWB radar uses this same principal, but uses an extremely short pulse across a wide range of frequencies, as

opposed to emitting and receiving a single frequency [15]. These principles are also described in more detail in chapter 2.

UWB radar sensors have many features that make them strong candidates for use in underground coal mines. Primarily, like US, it is robust to conditions of smoke, fog, dust, rain, snow, gas, and aerosols, but is more accurate and has higher resolution and range than US [9, 15, 16]. This is a key requirement as a result of the harsh conditions present in underground coal mines. Due to the low duration pulses used in UWB sensors, power consumption is small, typically below 1 Watt [17], a necessity in this application as high power consumption will lower the flying time of the drone significantly. Further, due to the nature of ultra-wideband emissions, the power spectral density of the sensor is very low, indicating minimal interference with any other wireless electronics such as the flight controller and associated telemetry link [17]. UWB radar can also provide a greater wealth of knowledge, meaning that more than just the distance to the nearest obstacle can be detected. This sensor can identify various features such as edges, corners, and walls, as well as provide three dimensional coordinates for the nearest detected object [18]. Finally, as UWB encompasses a large bandwidth of radio waves, it is more robust to a variety of targets; some objects will reflect differing amounts of radio waves dependent on the frequency, so having multiple frequencies present increases robustness to this error [17].

In industry as well, radar has been growing in popularity particularly with automotive manufacturers [16]. Most modern luxury cars now have adaptive cruise control or active brake assist features that utilize radar sensors; Audi, BMW, Cadillac, Lexus, and Mercedes all offer these features through the use of radar sensors [15]. This trend is due primarily to the robustness, range, and accuracy of these radar sensors relative to alternative options [16].

These many features of UWB led to its selection for further exploration in this thesis. The primary downside to UWB radar is that, as a relatively young technology, it is not as readily available in commercial off the shelf packages and is relatively expensive, especially compared to established sensors like US and IR. Nonetheless, this is acceptable for the purposes of this study, and will likely become less of an

issue over time. This thesis hopes also to contribute to the growing popularity of these sensors, accelerating the rate at which it becomes a more commercially viable option. Ultimately, the strong robustness to inclement conditions, high accuracy and resolution, available wealth of knowledge from the sensor, and low power consumption made this sensing method the best option. This thesis aims to experimentally validate and expand upon the usefulness of UWB radar for autonomous drones in the underground coal mine environment.

1.3 Thesis Contribution and Organization

There are two main contributions made in this thesis. The first is to validate that UWB radar performance remains strong in dusty and humid environments, both in static and dynamic cases. Though various studies have tested UWB radar in smoky conditions or simulated UWB radar use in harsher environments [15, 18, 19], this study aims to experimentally demonstrate the robust performance of this sensor extends to coal dust and humidity, both up to the levels typically present in coal mines. Second, this thesis will also verify experimentally that mounting a UWB radar sensor on a drone will not affect performance. Various studies analyze UWB radar on ground-based vehicles or suggest a potential application in drones [9, 15, 16, 17], and this thesis will validate that placing an UWB radar on a drone will not cause any drop in sensor performance.

This thesis is organized as follows. Chapter 2 describes the basics of radar sensors, and what distinguishes UWB radar from conventional radar. Chapter 3 discusses characterizing tests performed with the selected UWB radar sensor, the Walabot. Chapter 4 describes tests on the Walabot performed in adverse environments with a stationary target. Chapter 5 shows the tests performed on the Walabot in adverse environments with a dynamic target. Chapter 6 demonstrates potential error sources from placing the Walabot sensor on a drone and the tests that indicate these error sources are negligible.

Chapter 2

Radar

In this chapter, the operating principles of radar systems are presented. The specifics of UWB radar, and its differences from conventional radar, are also discussed.

2.1 Radar Principles

Radar, an acronym for RAdio Detection and Ranging, is a type of sensor that can detect the location of a target by transmitting and receiving reflected radio waves. Radio waves are emitted from the radar, propagate through the air, reflect off a target, and propagate back to the radar, where they are detected. From the time of flight and orientation of the detected radio waves, the location of the target can be calculated. Radio waves are defined as electromagnetic (EM) waves with frequencies ranging from approximately 1×10^3 Hz up to 1×10^{12} Hz [20].

The first step in a radar system is the emission and subsequent reception of radio waves, performed by a mechanism called the antenna. Though many different antenna designs exist, all function using principles from Maxwell's equations; sending an oscillating current through a wire will generate an oscillating electric and magnetic field around it [20]. By controlling the frequency of the oscillating current, an electric and magnetic field of a particular frequency can be generated around it. As such, when oscillating currents of radio frequencies pass through an antenna, an oscillating EM field will be generated around the antenna that will radiate away, creating emitted

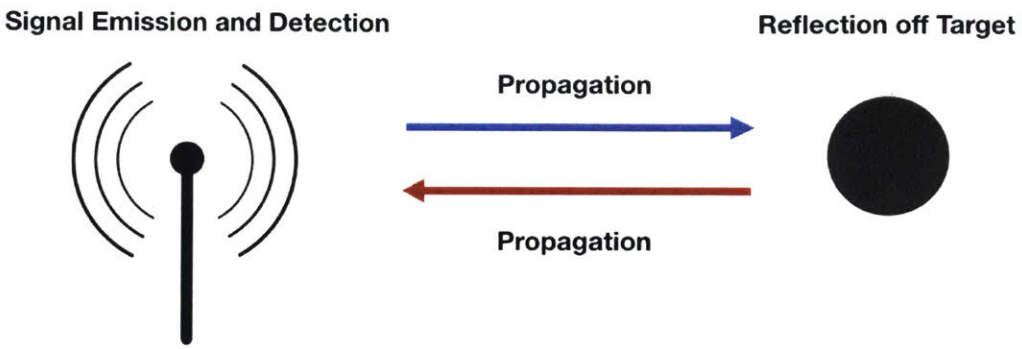

Figure 2-1: Simple radar system

radio waves. Typically, the antenna is designed to resonate at a particular frequency based on the length of the antenna, to increase the power and range of the emitted radio wave [20]. By the same principles, when a radio wave strikes an antenna, it will excite the electrons in the wire to generate a matching current, allowing incoming radio waves to be detected.

After an antenna emits a radio wave, this wave must propagate through the air to the target. EM waves will travel at the speed of light through a vacuum, and will slow down depending on the permittivity and permeability of the media through which it travels [20]. Air has a permittivity and permeability close to that of a vacuum, and the speed of light is typically used as a reasonable approximation of the traveling speed of radio waves through air.

The radio waves, upon reaching the target, will then follow the same laws of reflection and refraction all EM waves obey. When an electromagnetic wave hits the boundary between two mediums, a portion will reflect back and a portion will be transmitted through at a different angle [21]. This interaction is governed by the Fresnel equations and Snell's Law [21]. The Fresnel equations summarize how much incident power is reflected, r, and how much is transmitted, t, while Snell's Law determines the refraction angle of the transmitted wave. These factors all rely on the material properties of the two mediums and the frequency of the EM wave. Figure 2-2 illustrates these interactions for a simple, planar boundary between two mediums.

For the purposes of radar systems, these reflection factors are all summarized in

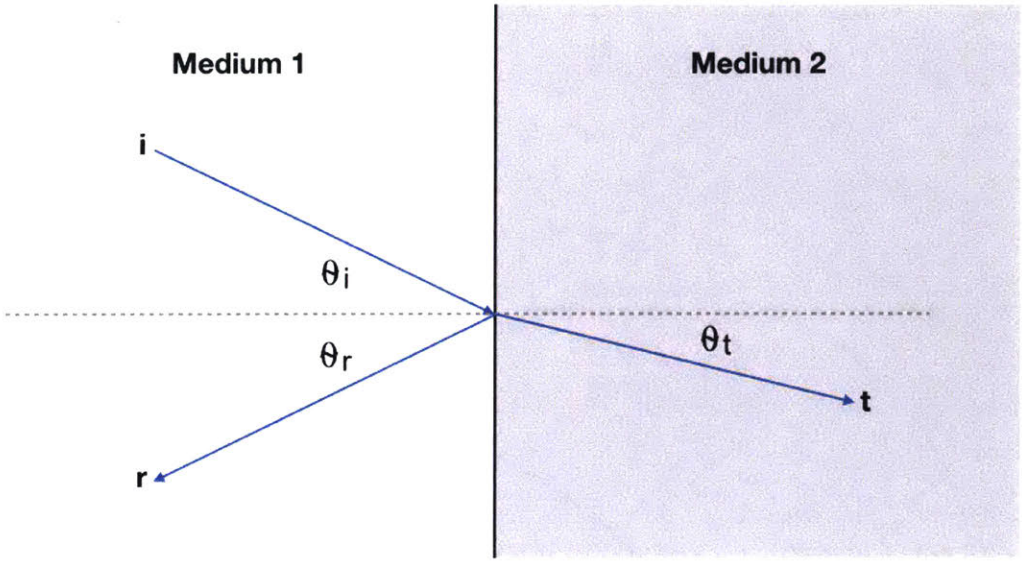

Figure 2-2: Reflection and refraction of an EM wave at a boundary

the radar cross section, σ. This factor indicates, for a particular target in a particular orientation, what fraction of the signal power is reflected back toward the receiving antenna.

The radar range equation is a fundamental component in describing the range of a radar system. It is used to determine the distance radio waves can propagate to a target before the signal power is too low to be detected. If we picture an isotropic antenna that is radiating in all directions, the signal power density for this isotropic case, $P_{d,i}$, at a radius R for a radar system with peak power P_{peak} will be [20]:

$$P_{d,i} = \frac{P_{peak}}{4\pi R^2} \tag{2.1}$$

However, a focusing antenna is often used that will concentrate the beam of radio waves in a particular direction. In these cases, there will be a dimensionless gain factor, G, in the range equation, shown in equation 2.2. This effect is illustrated in Figure 2-3 below. This focused signal power density, $P_{d,g}$, is given by [20]:

$$P_{d,g} = \frac{P_{peak} G}{4\pi R^2} \tag{2.2}$$

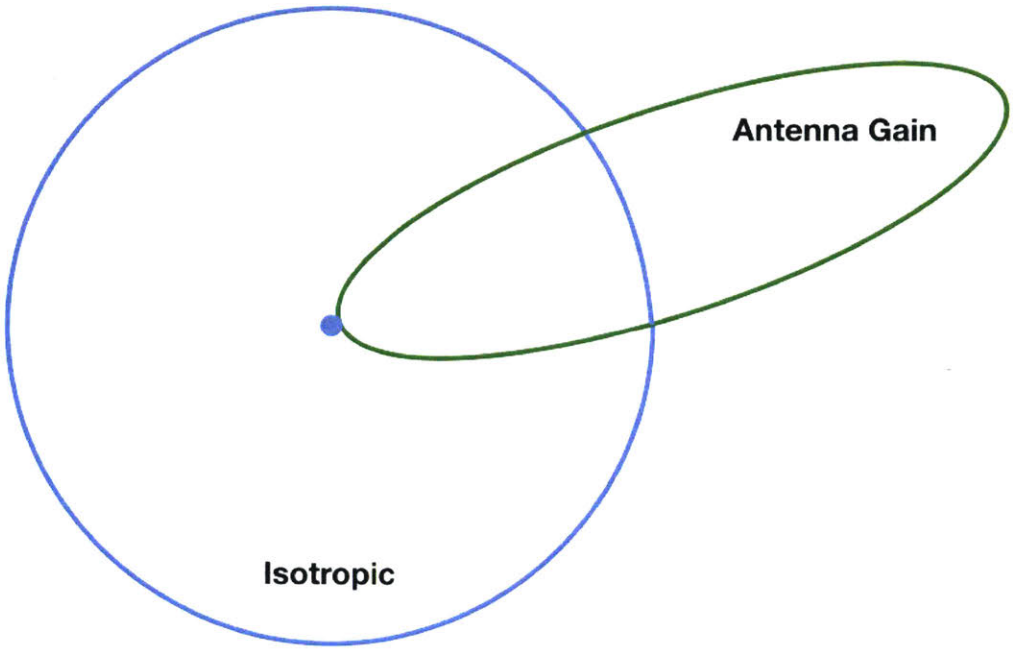

Figure 2-3: Isotropic radiation compared to antenna with focused gain

After the radio waves are reflected, the returning signal power will include the radar cross section, σ. As discussed before, this factor indicates the portion of the radar beam that is reflected after striking the target, and has units of m^2. The power reradiated back to the radar from the target, P_b, is given below [20]:

$$P_b = \frac{P_{peak} G \sigma}{4\pi R^2} \tag{2.3}$$

Then, once the signal is reflected, it must travel the same distance back to the radar system, assuming the transmitter and receiver are located in the same place. This means another factor of $4\pi R^2$ must be added into the denominator, as the radio waves must propagate distance R from the target back to the radar system. As

a result, the returning signal power density, $P_{d,r}$, is given by equation (2.4) below, typically referred to as the radar range equation.

$$P_{d,r} = \frac{P_{peak} G \sigma}{16\pi^2 R^4} \tag{2.4}$$

2.2 Ultra-Wideband Radar

UWB radar is a subset of radar systems that have relatively large bandwidths [22, 23, 24]. Conventional narrowband systems transmit continuous waveforms at a specific frequency, resulting in a small bandwidth and high power spectral density. UWB systems transmit brief, impulse-like waveforms, resulting in a large bandwidth and a low power spectral density spread out across a large range of frequencies. Figure 2-4 illustrates a simple, conceptual comparison between narrowband and wideband systems. Due to this low power signal, to a conventional narrowband system an UWB pulse would be difficult to detect as the signal power level is likely below the noise floor of a narrowband radar. The pulse width in UWB systems is usually between 100 picoseconds and a few nanoseconds, which corresponds to a frequency range of several GHz [24].

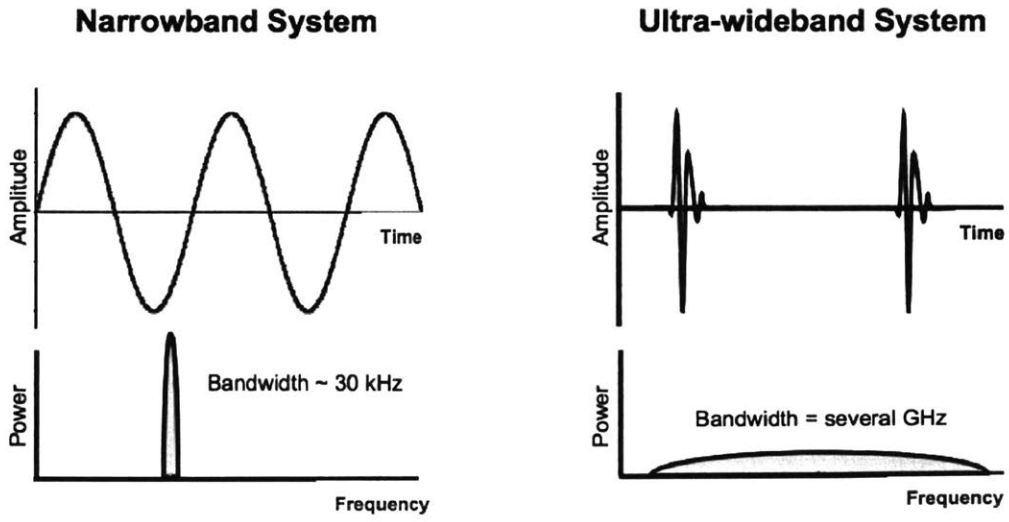

Figure 2-4: Comparison of narrowband and wideband radar systems [24]

The larger bandwidth results in different characteristics and applications for UWB systems with regard to narrowband systems. Primarily, as equation (2.4) illustrates, having a lower peak power reduces the achievable range of the sensor. If the returning signal power density is too low, it cannot be reliably detected. UWB radar systems are commonly used in short range applications, on the order of meters, in comparison to narrowband systems which can achieve ranges on the order of kilometers [24, 20]. However, this also means that UWB systems consume much less power. As a result, this makes UWB radar more feasible for portable, low-power systems. In simple terms, UWB can be thought of as a low-power, short range radar system. This makes it ideal for use as a sensor on a drone; UWB radar can provide the accuracy, resolution, and detail of a typical radar system, but with low power consumption and a shorter range.

2.3 Summary

Radar systems are capable of detecting targets by emitting radio waves and then receiving the reflected waves. From the time delay between the emitted waves and the received reflected waves, the distance to the target can be calculated. Conventional radar systems use a narrowband technique, where a single frequency signal is emitted. This results in a high power, low bandwidth system with a long range. UWB radar instead opts to use brief impulse signals that have high bandwidth and low power, resulting in a shorter range. As a low power, short range radar system, UWB radar is a strong candidate for application on drones.

Chapter 3

UWB Radar Sensor Characterization

This chapter describes a series of characterizing tests performed on a representative UWB radar sensor, the Walabot Pro. The primary goal of these tests is to characterize the performance of this sensor in ideal conditions, to ensure that it functions as expected. The accuracy, resolution, and repeatability of the sensor are analyzed in several scenarios.

3.1 UWB Radar Sensor

The Walabot Pro UWB Radar sensor was selected as the robust sensor for use in this study. The Walabot sensor is relatively low-cost at $600 but is still fully programmable and developer friendly, with an SDK kit that is compatible with Windows, Linux, Android, and Raspbian. The US model of the sensor operates at the FCC approved frequencies of 3.3-10.3 GHz, and connects to a computer via microUSB.

The sensor is approximately the size and weight of a modern smartphone, with dimensions 145 x 85 x 18mm, and a weight of slightly under 140g. The sensor does not have onboard processing capabilities, and so relies on the connected computer for control and power. Walabot consumes 2-4W of power, varying with the user-defined arena, resolution, and operation mode. The sensor has a conical arena that can reach up to 15 meters with a FOV of $\pm$ 45 degrees in both the horizontal and vertical directions. The resolution will vary greatly with the many user-controlled options,

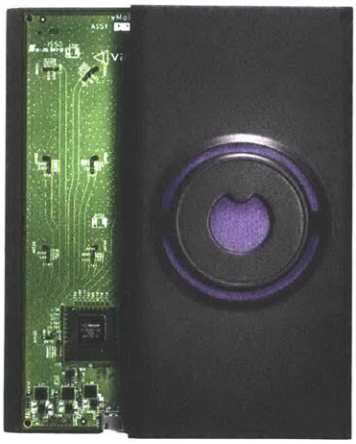

Figure 3-1: Walabot Pro ultra-wideband radar sensor [25]

but a resolution on the order of millimeters can be achieved.

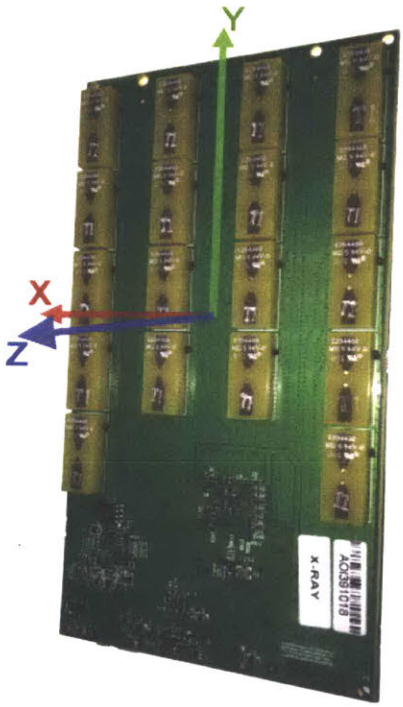

Figure 3-2: Internal board of the Walabot Pro, with axis definitions [25]

Figure 3-2 shows the internal board of the Walabot Pro sensor, with the axis definitions illustrated. This image shows the back of the board, such that in Figure

3-1, the Z axis would be pointing into the page. The board contains 18 separate antennas with transceiver capabilities to increase the resolution of the readings.

The main goal in selecting the Walabot sensor was to use it to experimentally validate the robust nature of UWB radar sensing, and it fulfills these needs well. However, for implementation on a drone, a smaller footprint, reduced power consumption, and reduced mass would be important factors to consider to ensure the drone can maintain the required flight time and payload characteristics. Though this was not tested experimentally, the Xethru X2 SoC was identified as a UWB radar sensor with strong potential for drone implementation.

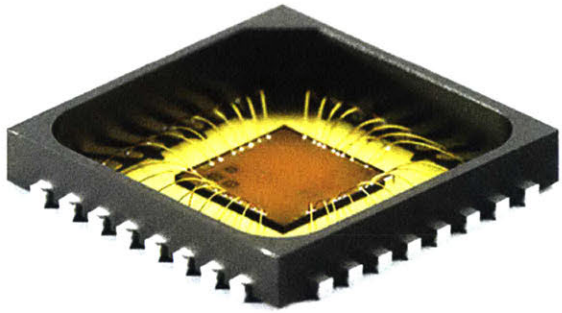

Figure 3-3: Xethru X2 SoC ultra-wideband radar sensor [26]

The X2 boasts strong specifications, with a power consumption below 120 mW, sub-mm accuracy, and a range of up to 30m, all within a single chip package measuring 5.6 x 5.6mm and a cost of $65 per chip. Though not ideal for this study, as the chip is not developer friendly nor easy to program, the X2 is the ideal candidate for production level implementation on a drone. It illustrates that if the UWB radar sensing method is indeed robust to the adverse conditions of a coal mine, a sensor that is small, light, and low-power enough to be implemented on a drone is already commercially available.

3.2 Radial Accuracy Testing

First, a few simple characterization tests were performed with the sensor, primarily to ensure that sensor performance is accurate enough, and repeatable enough, to make

worthwhile conclusions in the later portions of this study. If the sensor is too noisy, or too inaccurate, it won't be possible to reliably compare sensor readings in normal to adverse environments, as the sensor noise would drown out any changes caused by the adverse environment. Of particular importance is the repeatability of the sensor, as the main goal of later tests will be to compare sensor readings in normal environments to adverse environments. If the sensor is precise, even if the readings are inaccurate, it will make for a reliable comparison.

For this test and all future tests, the Walabot radar sensor was programmed to track the two targets with the highest reflected power. The sensor, using sample code obtained from the Walabot SDK, is programmed to perform the necessary signal processing to piece together the raw data from all antennas to calculate the center of the detected target. For the purposes of this study, the sensor was additionally programmed to record a timestamp for each data point, and to assemble all of the data into a single spreadsheet for each trial. Ultimately, this means that after every trial, a spreadsheet was saved containing ten columns; the time, x value, y value, z value, and reflected power, each for the two targets.

Two separate sensor operating modes are used in this study to track static and dynamic targets. For all tests except those in chapter 5, the static operating mode is used. When operated in this mode, the sensor initializes upon startup to the current environment by taking a reading of its environment. After initialization is complete, it will compare all successive readings to the initialization reading to detect a change. This allows the sensor to detect when a target is placed in front of it, while ignoring walls or any objects in its view other than the desired target. In chapter 5, when dynamic targets are analyzed, the sensor applies a moving target identification filter (MTI) that removes static signals. In this mode, the sensor compares current readings to the previous reading and ignores any targets that have not moved from one frame to the next.

For all tests in this chapter, a conical arena extending 5m with $\pm$ 25 degrees in both the horizontal and vertical axes was defined.

The first characterization test performed was designed to test accuracy at various

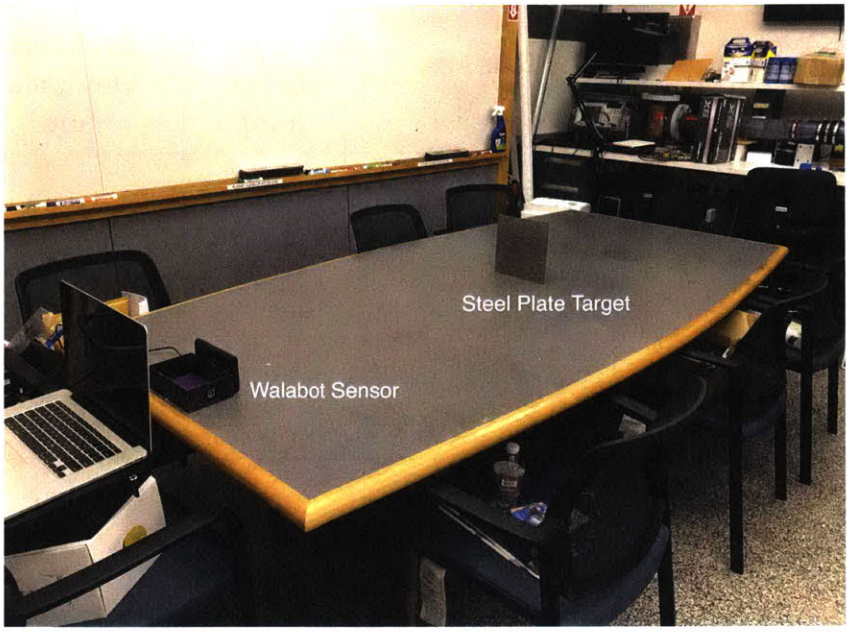

Figure 3-4: Image of test setup for radial testing

ranges. After initializing to the empty room, an 8in square steel plate was placed at various distances, directly in front of the sensor, as shown in Figure 3-4. This steel plate was used as the ideal sensor target, as metals are highly radar reflective and the large plate has a high surface area, ensuring the radio waves will reflect back to the sensor. At each distance, over 1000 data points from sensor readings were recorded, and the results are tabulated below. In this test scenario, the radar sensor has strong repeatability, on the order of millimeters, and acceptable accuracy, on the order of centimeters.

Table 3.1 shows only data for the Z axis, as this testing was focused on the radial distance between the target and the sensor. The target was placed directly in front of the sensor, at various distances, and 1400 data points were collected in each test. The true distance is the measured distance from the sensor to the target. The average measured value is the average of all sensor data points. The range shows the minimum and maximum values recorded by the sensor. The delta range is the difference between the maximum and minimum recorded values. The standard deviation is a measure of the variability of the data set. The absolute error is the error between the average measured value and the true measured distance. The calculations used to determine

True Distance [cm]	Average Measured Value [cm]	Range [cm]	Delta Range [cm]	Standard Deviation [cm]	Absolute Error [cm]
75	78.686 ± 0.002	78.55 - 78.33	0.29	0.045	3.686
100	101.488 ± 0.002	101.38 - 101.61	0.22	0.032	1.49
150	152.072 ± 0.001	151.99 - 152.17	0.18	0.024	2.07
200	78.686 ± 0.002	200.86 - 201.36	0.51	0.038	1.20
250	78.686 ± 0.002	251.19 - 251.43	0.25	0.038	1.31
300	78.686 ± 0.003	299.63 - 301.05	1.42	0.062	0.86
400	400.688 ± 0.031	398.49 - 402.79	4.30	0.573	0.70

Table 3.1: Table containing data from Walabot radial accuracy testing. Uncertainty range represents 95% confidence interval.

the standard deviation and 95% uncertainty range are shown in Appendix A.

As this data demonstrates, in these conditions the radar sensor is highly repeatable. The maximum delta range seen is only 1% of the measured value, meaning the sensor noise is within 1% of the average value with over 1000 data points recorded. The 95% confidence intervals for the true measured mean are incredibly small, all except the final test are on the order of tens of microns, and all except the last test have standard deviations of less than a millimeter.

The last test, at 4m, was noticeably less repeatable than other tests, with a larger 95% confidence interval, delta range, and standard deviation. This is likely due to the fact that 4m was almost the full length of the room, and at 4m the target was placed on the table in the back of the image above. There were more objects on the table cluttering the sensor's view and adding reflections other than the target, effectively raising the signal noise barrier, resulting in the lower repeatability. That being said, this test still maintained a 95% confidence interval of less than half a millimeter, illustrating that the sensor has very strong repeatability nonetheless.

There is a loose trend of increasing accuracy as the target moves farther away. There are two likely causes for this trend. First, as the target moves away, the time of flight for the radio waves increases. With a fixed time resolution in the receiver antenna, a longer time of flight will result in a more accurate measurement. Second, as the target moves away, it takes up a smaller portion of the sensor's arena, reducing the affects of multipath errors. When the target is close and takes up a large portion of the sensor's view, there are more potential paths for radio waves to reflect back to the sensor, causing a multipath error in the sensor's reading.

The readings are nonetheless reasonably accurate, always within 4cm of the true value, and typically within 1-2cm. This is an acceptable accuracy level for the purposes of this study.

3.3 Three Dimensional Accuracy Testing

As an addition to the previous tests that only analyzed radial accuracy, a similar test was performed to determine the accuracy along all three axes. The same test method was used, except that the steel plate target was placed at an arbitrary location, and then data was analyzed for all three axes of the sensor. The resulting data is show in Table 3.2. All of the column definitions are the same as those in Table 3.1.

Axis	True Distance [cm]	Average Measured Value [cm]	Range [cm]	Delta Range [cm]	Standard Deviation [cm]	Absolute Error [cm]
X	**22.5**	21.649 ± 0.009	20.97 - 22.42	1.45	0.147	0.85
Y	**34**	33.122 ± 0.007	32.68 - 33.48	0.80	0.118	0.88
Z	**172.5**	173.149 ± 0.003	172.93 - 173.38	0.45	0.048	0.65

Table 3.2: Table containing data for the Walabot 3D accuracy testing. Uncertainty range represents 95% confidence interval

In this test, the target was placed at an arbitrary location a little under two meters away and oriented facing toward the sensor, and 1400 data points were again

collected. The true measured distance was obtained by using a tape ruler to measure the distance from the sensor to the target.

The data for the x and y axes is slightly less accurate and slightly less repeatable than in the z axis. This is likely due to the fundamental difference in the method the sensor uses to measure along these axes. The sensor obtains data about the target in spherical coordinates, using time-of-flight to determine the radial distance r, and measuring incident angles of the radio waves on the receivers to measure ϕ and θ. These two variables are defined, respectively, as the angle from the x axis on the x-y plane and the angle from the z axis on the y-z plane. The distance along the Z axis in most cases will depend mostly on the radial distance r, while x and y will depend primarily on ϕ and θ, causing this variation in accuracy and repeatability. Further, x and y will also depend on the capability of the signal processing algorithm used by the radar sensor to calculate the center of the target, which will also add error to the measurement.

Nonetheless, the measurements along all three axes are still strongly repeatable, with 95% confidence intervals on the order of microns, standard deviations around 1mm, and accuracy of around 1cm.

3.4 Resolution Testing

As a final step in characterizing the radar sensor performance, the resolution of the sensor in these conditions was determined. The same test as those in sections 3.1 and 3.2 was performed, except that in this case the steel target was placed on a precision optical stage, as shown in Figure 3-5, which was moved in 1mm steps. At each step, 200 data points were recorded and analyzed.

To determine the resolution, the full range of the 200 data points at each step is represented in the error bars in Figure 3-6 below. Once the error bars no longer overlap, this indicates that with a single data point, the step could be read by the sensor with 100% confidence. This was defined as the sensor resolution for this test; the point at which the range of the sensor at two points stop overlapping.

Figure 3-5: Image of steel target on optical stage for resolution test

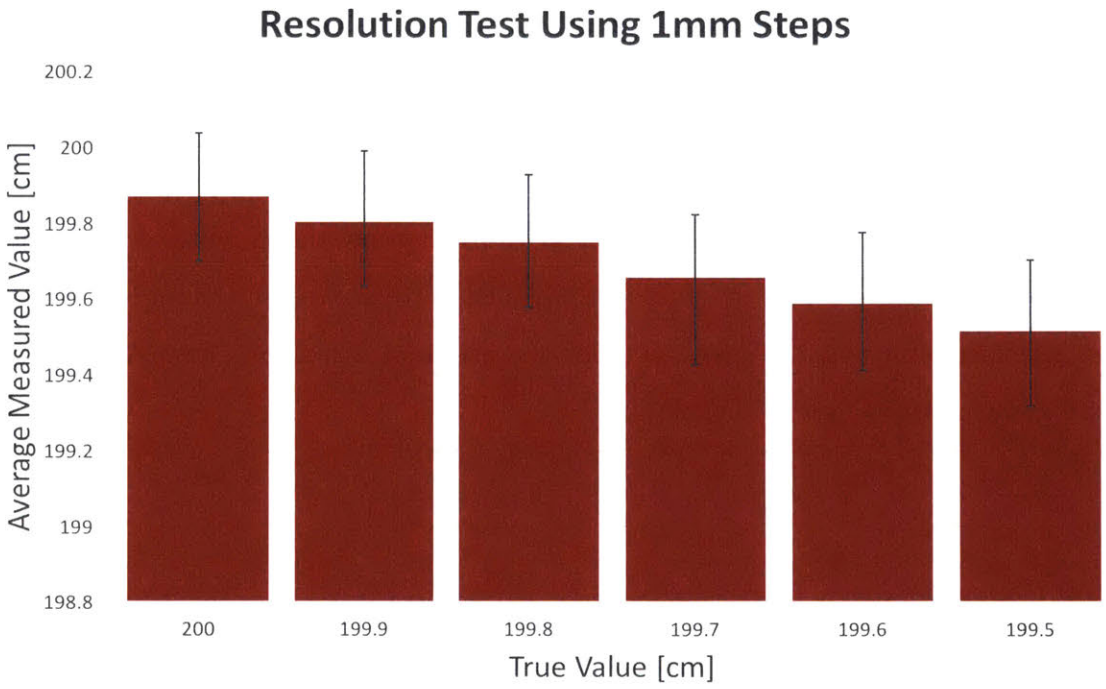

Figure 3-6: Resolution test data from the Walabot sensor, 1mm steps. Error bars represent full range of sensor data

Figure 3-6 demonstrates the results of the resolution test described above. After initializing the radar sensor without the target in its view, the steel target was placed 200cm away, directly in front of the sensor. The target was placed on top of a precision optical stage. After 200 data points were collected in the first position, the stage was stepped 1mm closer to the sensor. After 200 more data points were collected, the

process was repeated until the target was 199.5cm away from the sensor.

The bottom edge of the 200cm error bar and the top edge of the 199.5cm error bar are both at 199.70cm, so this is the point at which the error bars no longer overlap. This illustrates that, as discussed before, the smallest step the sensor can reliably detect with a single data point is 0.5cm.

This resolution is quite strong, but it must be noted that these tests were performed in ideal conditions. In later chapters, the sensor will be tested in harsh conditions, and it should not be expected that all experiments performed will achieve this level of repeatability, resolution, and accuracy.

3.5 Summary

The Walabot Pro UWB radar sensor is a low-cost, lightweight, and low-power sensor that was selected for this study. In ideal conditions, this sensor has very strong accuracy, resolution, and repeatability. The Walabot consistently achieved accuracies on the order of cms up to a range of 4m and a resolution of approximately 0.5cm, all with a repeatability on the order of microns. In good conditions, the Walabot is a capable sensor with good performance.

Chapter 4

Static Target Detection in High Dust, Humidity

In this chapter, the robustness of the sensor was examined when detecting a static target with vision obscured by high dust concentrations and high levels of humidity. The objective of this chapter is to experimentally illustrate that the Walabot sensor is capable of detecting a static target through the dust and humidity levels commonly seen in a coal mine.

4.1 Experimental Design and Goals

To create a contained test environment with controlled conditions, a test setup was assembled inside an acrylic box measuring approximately 40 x 40 x 40cm. Five fans, two humidity sensors, and two dust sensors were placed inside the box to measure the conditions inside the test environment. Detailed data on each of these can be found in Appendix B. Brushless fans were used to ensure no sparking occurred, which otherwise might ignite the coal dust. Weathering tape was then placed down around the top edges of the box, such that when the lid was clamped shut, the tape would compress and seal the opening to prevent dust or moisture from escaping during testing.

To mount the Walabot sensor in a fixed location on the outside of the box, four L shaped brackets were attached to the box in such a way to provide a slip fit for the

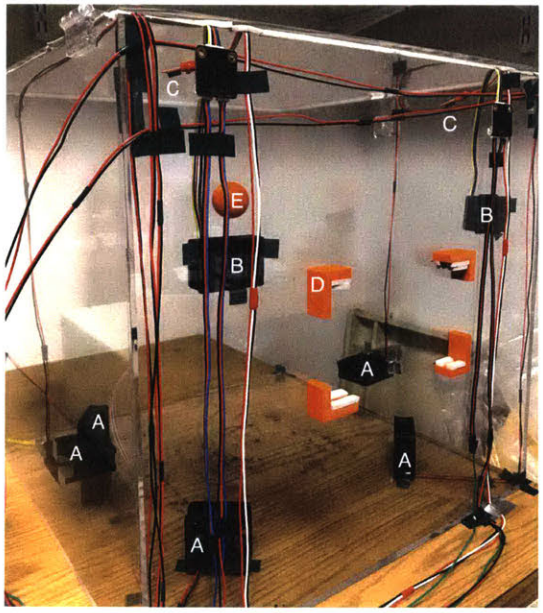

Figure 4-1: Adverse environment testing setup. A are fans, B are dust sensors, C are humidity sensors, D is radar mount, E is static target.

sensor, labeled D in Figure 4-1. Then weathering tape was placed around the edges of the brackets to ensure the sensor was stable and stationary. The friction from the compressed tape was sufficient to ensure the fit was stable and the sensor could simply be gently pressed into the slot, and gently pulled out after testing. The sensor was mounted outside the box to ensure the dust or moisture wouldn't penetrate the sensor and potentially damage it. As radar is capable of penetrating through acrylic well, this will protect the sensor without preventing it from detecting the target inside.

For a fixed target location, a small peg was attached to the inside of the box. Any hollow target could then simply be slipped onto or off the peg. For all tests in this chapter and the next, a spherical target was used, labeled as E in Figure 4-1. The orange mounting peg can be seen in Figure 4-2.

The primary goal of this testing is to illustrate, quantitatively, that the UWB radar sensor readings are unaffected by the addition of coal dust or moisture into the environment. To achieve this, the change in sensor readings when coal dust or moisture is added to the environment is compared to a control test. If the change from sensor readings during adverse tests is the same as the change in the control test, this indicates that adding the adverse environmental conditions does not significantly

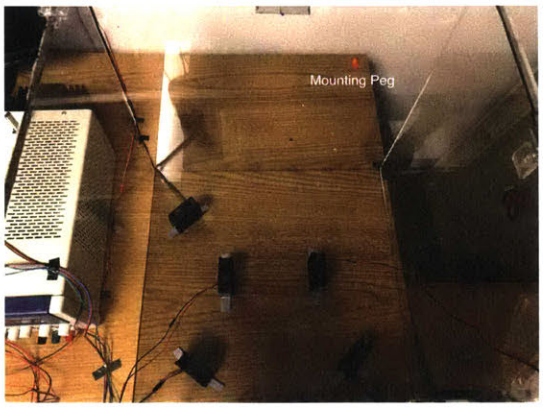

Figure 4-2: Testing environment from above during a coal dust test, showing final fan orientations and mounting peg

affect sensor performance. The control test will capture any change caused by sensor noise, multipath errors in the box that may amplify noise, vibrations from the fans, and any other errors that may affect sensor readings.

4.1.1 Humidity Sensor Calibration Verification

The chosen humidity sensors were the Honeywell HIH-4030 sensors. These small, low-cost sensors are basic humidity sensors, with an analog voltage output linearly corresponding to a relative humidity, in %. The rated accuracy of the sensor is $\pm$ 3.5% RH, with a repeatability of $\pm$ 0.5% RH. The sensors are factory calibrated and come with the slope and offset of the calibration curve. The data for these two particular sensors is in Appendix B. All calibration data is performed at 25°C, and all tests in this study were performed at room temperature, approximately 25°C as well.

To verify the factory calibration of the two ordered sensors, the "salt test" was performed. This is a common test used to check humidity sensor calibration, utilizing the fact that a saturated solution of table salt (NaCl) will generate a humidity of precisely 75% in a contained environment [27].

The two sensors were placed in a sealed bag with a saturated solution of table salt, and left to stabilize for 48 hours, as shown in Figure 4-4. The sensor readings were then recorded, and are shown in Table 4.1.

Humidity sensors 1 and 2 are shown in Figure 4-4. As the data in Table 4.1 shows,

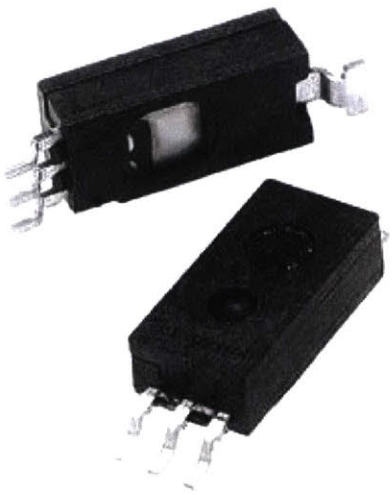

Figure 4-3: Honeywell HIH-4030 humidity sensor

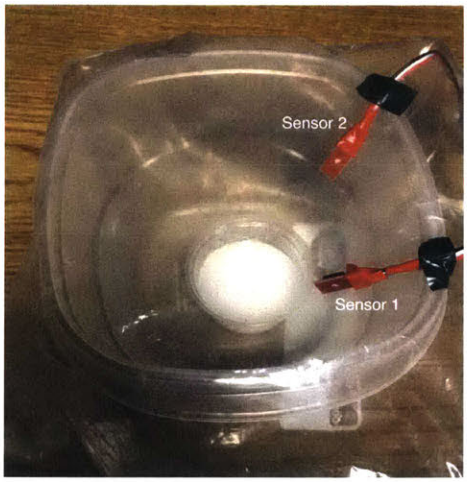

Figure 4-4: Humidity sensor salt test

Sensor Number	**Analog Voltage Reading [V]**	**Calculated Humidity [%RH]**
1	3.14	74.70%
2	3.12	74.32%

Table 4.1: Table containing salt test humidity sensor data

the humidity sensor calibration data is quite accurate, and well within the ± 3.5% RH rating, so the given calibration data will be used for all testing.

4.2 Determination of Dust Concentration

Determining the airborne coal dust concentration proved a more challenging task. All low cost dust sensors found had a limited range, with a maximum at 0.5 mg/m^3, and this study aims to reach coal dust concentrations of 4 mg/m^3, as mentioned in Chapter 1. Other dust sensors were either prohibitively large or prohibitively expensive, costing several thousands of dollars. So to reasonably estimate the dust concentration up to 4 mg/m^3, several videos were taken of the test setup during coal dust testing and then analyzed. Using image processing, the frames with dust were compared to those without dust to quantify the change in pixel intensity. This change in pixel intensity was correlated with a dust sensor for values below 0.5 mg/m^3, and then using that model, dust concentrations for values above this limit were calculated using pixel data from corresponding videos.

Figure 4-5: Sharp GP2Y1010AU0F optical dust sensor

The Sharp GP2Y1010AU0F Optical Dust Sensor was selected as the low cost dust sensor to be used. The sensor outputs an analog voltage that corresponds linearly to dust concentration. The sensor has a sensitivity of 0.5V per 0.1mg/m^3, and the offset was set through a zero-calibration in a dust free area, ensuring that the sensor output reading is zero when no dust is present. The sensor utilizes an infrared emitting diode and a phototransistor to detect when dust is present, and is commonly used in air

purifiers or air monitors.

For the coal dust itself, powdered coal dust was purchased from Peco. The part number for the chosen dust is PecoScene PS-362 Coal Dust. This dust is marketed as a weathering powder, to make small models and replicas of trains or trains stations appear more realistic. Though this intended purpose is far from the one in this study, the low cost and available small quantities made this the most viable option. Small quantities, below 50g of coal dust were required for this study, and all other options required purchases on the order of several kilograms or more. After initial testing found these particles too large to become easily kicked up by the fans' airflow in the test environment, this dust was ground down slightly in a mortar and pestle before use, both to allow more of the dust to become airborne and to provide a more consistent particle size.

For the video data, an iPhone 7 camera was used to film video at 30 frames per second, with 1080p HD resolution. First, recording was started with the fans inside the test environment off, with all the coal dust resting on the floor. A few seconds into the video, the fans were turned on, kicking the dust up into the air. After a few more seconds, recording was stopped.

This video was then imported into MATLAB for data analysis. First, the video was separated into individual frames, and then each frame was converted to a grayscale image. Converting to grayscale simplifies the comparison between frames by combining red, green, and blue (RGB) data into a single value representing pixel intensity. This pixel intensity is recorded in MATLAB as a value between 0 and 255, where 255 represents a perfectly white pixel, and 0 represents a perfectly black pixel. Figure 4-6 shows a comparison between the first and last frame in one of the coal dust videos, illustrating the change in grayscale pixel intensity caused by the airborne coal dust. The images in this figure were taken from the video of the coal dust test with 24g of dust in the box.

The video was then processed to quantify the change in pixel intensity caused by the addition of dust. The MATLAB code used is shown in Appendix C. For each video, the first frame is taken as a baseline value. The average of every pixel

Figure 4-6: Comparison of first and last grayscale frames in 24g coal dust testing video

intensity value in the frame is taken, resulting in a baseline average value. Then, for every subsequent frame in the video, the grayscale pixel intensities are again averaged and subtracted from the baseline average value, resulting in an array of values representing the change in pixel intensity for each frame. It is expected that as the dust concentration increases, the average pixel value will decrease, as the darker a pixel is, the lower its intensity value is. As such, this relative change was always recorded as the baseline average minus the current frame average, so that an increasing value corresponds to an increase in coal dust. This relative change of the average pixel intensity was then plotted with respect to the frame number, resulting in plots similar to that of Figure 4-7. This figure is for the 24g coal dust test video, matching the image data shown in Figure 4-6. After the fans were turned on, the change in pixel intensity increases until it reaches a steady state value.

Next this graph was further analyzed to calculate a single value representing the net change in pixel intensity caused by the dust. For Figure 4-7, it is clear the fans were turned on at approximately 90 frames into the video, or three seconds after recording began, as this is when the relative pixel intensity starts to increase. To

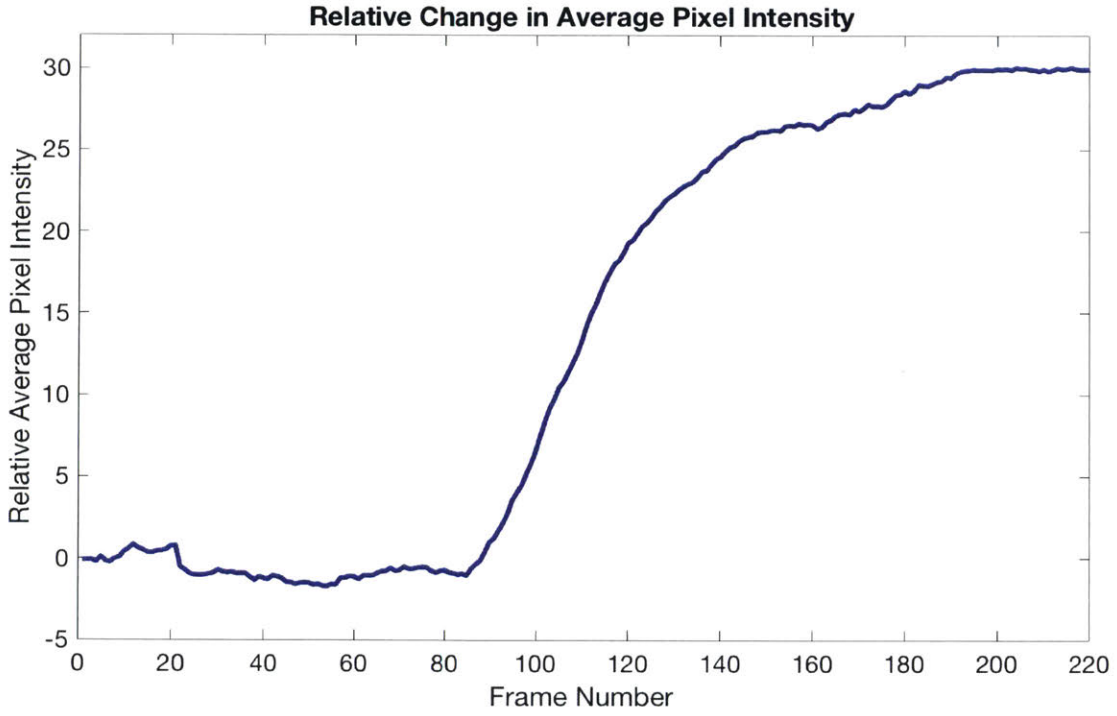

Figure 4-7: Representative plot for the change in pixel intensity caused by coal dust, with respect to the frame number of the video

calculate the net increase in pixel intensity after reaching steady state, 30 frames were averaged from the start and end of the video, and then the difference between the two was calculated. For example, in Figure 4-7, frames 50 through 80 and frames 190 through 220 were averaged, and the difference between these two values was recorded as the average increase in relative pixel intensity caused by coal dust. An associated 95% confidence interval for this value was also calculated using the standard deviation of the averaged pixel data.

Then, the next step was to determine the relationship between this change in pixel intensity and a physical dust concentration. For each video taken, data was also simultaneously collected from the Sharp dust sensor. After the dust concentration stabilized, 50 data points from the dust sensor were averaged, and a 95% confidence interval was calculated based on the standard deviation of the data points. Six different video dust tests were performed at dust levels below the sensor saturation value of 0.5 mg/m^3, and the resulting dust sensor data is plotted in Figure 4-8, with

the net change in relative pixel intensity plotted on the x axis and the average dust sensor concentration plotted on the y axis.

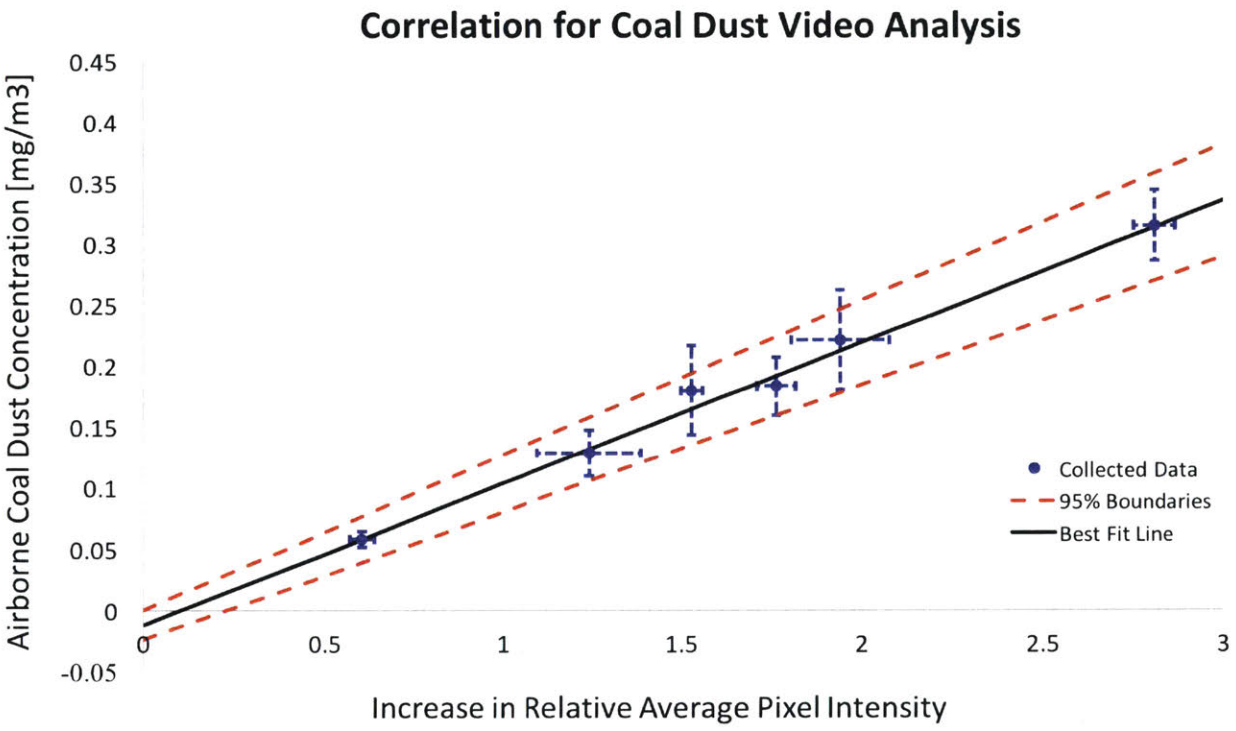

Figure 4-8: Correlation between net increase in relative pixel intensity and airborne dust concentration

A linear regression of the six data points was performed, and the results are also plotted on Figure 4-8, with the black line showing the best fit curve, and the dotted red lines indicating the 95% confidence interval of the best fit curve. A linear regression was selected both because it fits the data well and it is logical that if twice as many pixels are darkened then twice the amount of dust is present. The offset value is expected to be zero, because if there is no change in the pixel intensity, this indicates that no dust is present. Though the best fit line has a small zero offset, zero is included in the 95% confidence interval.

This best fit line has now given us a method to use video data to calculate airborne coal dust concentrations beyond the limit of the dust sensor. This can now be used to reasonably estimate the coal dust concentration in the test environment up to the desired 4 mg/m^3.

Radar sensor testing was then performed at four different dust levels, with 8g, 16g, 24g, and 32g of dust present in the test environment, with videos taken at each level. However, only a small fraction of the dust in the test became airborne during testing, and all data from the dust sensor was saturated at all four levels. As such, the videos were analyzed using the same method described above, and using the linear regression data presented in Figure 4-8, the change in the relative pixel intensities was mapped to an airborne dust concentration value, and an associated 95% confidence interval. The resulting dust concentrations are shown in Table 4.2.

Dust in Test Environment	**Increase in Relative Average Pixel Intensity**	**Airborne Dust Concentration [mg/m^3]**
8g	16.11 ± 0.30	1.85 ± 0.23
16g	25.72 ± 0.10	2.96 ± 0.31
24g	31.13 ± 0.15	3.59 ± 0.38
32g	37.07 ± 0.31	4.27 ± 0.47

Table 4.2: Calculated dust concentration levels beyond dust sensor saturation

As the table above illustrates, the final test is approximately at the desired 4 mg/m^3 concentration level, indicating that the testing performed does indeed reach the peak level of dust concentration expected in the coal mine environment. The test environment is therefore creating a dusty environment that is comparable to those seen in a coal mine, to ensure the sensor testing matches the dust levels seen in a true mine.

4.3 Radar Sensor Data

To analyze the effect of adverse environmental conditions on the performance of the radar sensor, sensor performance was compared to a control scenario with no added dust or moisture. For all radar sensor tests in this chapter and the next, a conical

arena extending 1m with ± 25 degrees in both the horizontal and vertical axes was defined.

In this control scenario, the radar sensor was initialized to an empty box without a target present, as described in Chapter 3. Then, the orange, spherical target was placed on the peg inside the test environment. Data was recorded for 30 seconds, termed the 'start' data, and then the fans were turned on. After one minute with the fans on, data was then recorded again for another 30 seconds, termed the 'end' data. This was repeated five times, for all test scenarios.

Then, the same process was repeated with the addition of moisture or dust into the test environment. For example, with moisture, water was sprayed into the test environment when the target was added. After the fans were turned on, the humidity level in the box rapidly increased up to approximately 100% RH, taking approximately five minutes to stabilize at a saturated relative humidity. The same initial 30 seconds of start data was recorded, and then 30 seconds of end data was recorded after both humidity sensors read 99% RH or above.

For the coal dust testing, four different levels of dust were added into the box, as discussed at the end of section 4.2. For each level, the coal dust was measured and added in prior to any testing. Then the exact same process as the control was followed, with the only difference being that when the fans are turned on, they kick up the dust to create the desired dusty environment. Again, the same start data set was recorded initially, and after one minute to allow the dust concentration to reach a steady state, the end data set was recorded.

Each set of data includes a timestamp, x value, y value, z value, and reflected power value for the center of the detected target. To analyze this data, for each axis the change between the averages of the start and end data sets was calculated, along with a 95% confidence interval for that difference. 50 points from each data set were used when calculating averages and confidence intervals. Then, for each test scenario, the five differences from each of the five trials were averaged together, and again a 95% confidence interval was calculated.

This was calculated to isolate the changes in sensor readings caused by the adverse

environment. If the environmental conditions are affecting the sensor performance, then this would be reflected in a large change between the start and end data sets, relative to the control test. The control test captures any potential sources of error other than the specific adverse environmental conditions in the tests performed. The only difference between the control tests and the adverse tests is the added dust or moisture, so if there is a discrepancy between the delta values of the adverse tests, this discrepancy must be caused by the adverse conditions. If there is no discrepancy, this means that any non-zero delta values are caused by other sources of error, such as sensor noise, multipath errors, the acrylic box refracting transmitted radio waves, or vibrations caused by the fans, for example.

Initial data analysis for tests performed at 3.59 mg/m^3 and 4.27 mg/m^3 resulted in large error bars due to a few outlier data points. Five more trials were performed for each test scenario, and this additional data was more consistent, reducing the influence of these outliers.

As discussed in chapter 2, it is predicted that the coal dust will not affect the radar sensor performance, as electromagnetic waves at radio frequencies transmit through small dust particles well, due to the fact that only a small fraction of the power is scattered or reflected. Most of the wave transmits through unchanged. As a result, the expected outcome is that the calculated delta values for the test scenarios with adverse environmental conditions will be similar to the delta values from the control tests.

Figure 4-9 illustrates all the collected data for testing performed on the radar sensor with a static target. The columns are split into each axis, as the data from each axis was analyzed separately. The green column to the left represents the control, the light blue represents humidity data, and all the red columns represent coal dust data at the four levels described in section 4.2. The coal dust concentration increases from left to right, with the rightmost, brightest red column representing the highest coal dust concentration at 4.27 mg/m^3. The y axis in the figure represents the average delta value calculated between start and end data sets for the respective test scenario.

The main purpose of collecting the data in this figure, as mentioned before, is to

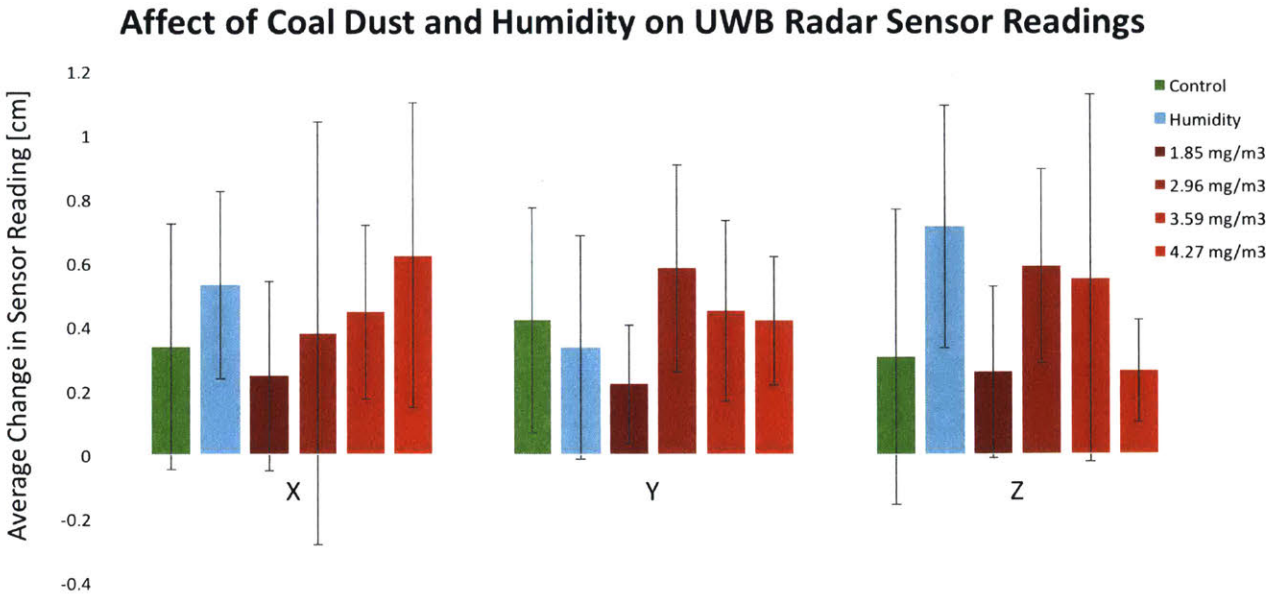

Figure 4-9: Results of static target radar sensor testing in adverse coal dust and humidity conditions. Error bars show 95% confidence intervals.

illustrate that the delta values for all five adverse tests fall within the error bars of the control data. This indicates that there is no significant change in the radar sensor performance caused by the addition of adverse environmental conditions, demonstrating that the predicted hypothesis is supported by the collected data. There is no environmental condition tested that caused a sensor error exceeding the error seen in the control test, when utilizing 95% confidence intervals. This implies that the radio waves in the frequency spectrum of the Walabot UWB radar sensor, 3.3 - 10.3 GHz, were successfully able to transmit through the tested levels of airborne moisture and coal dust.

However, this conclusion is limited by the size of the confidence intervals displayed in the error bars. No discernible trend can be seen, but this may be because the size of the error bars is masking it. In this case, the conclusion can nonetheless be reached that the effect of these adverse conditions is negligible. The maximum gap between the bottom edge of the lowest control error bar and the highest adverse test error bar is on the order of 1cm. This indicates that within the 95% confidence interval, the maximum possible change in the sensor readings caused by the addition of coal or

moisture is approximately 1cm. This value is still within acceptable accuracy levels for the purposes of obstacle avoidance, so even if there is a trend too small to be seen in the range of test data collected, it cannot exceed a sensor error of 1cm.

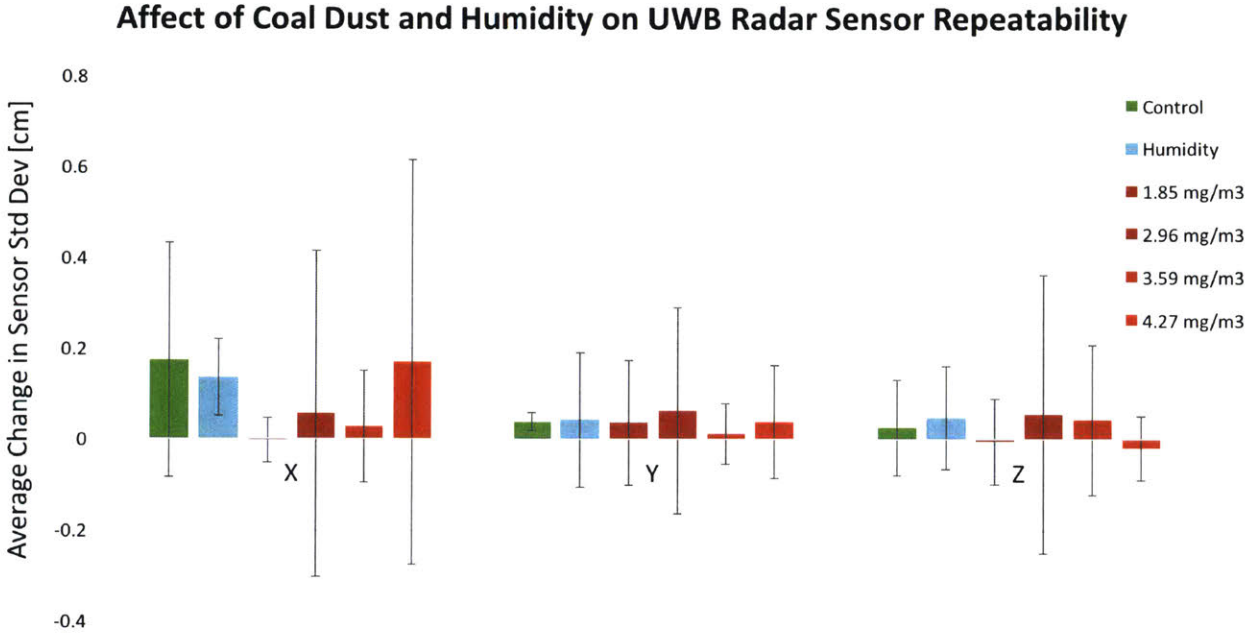

Figure 4-10: Results of static target radar sensor repeatability testing in adverse coal dust and humidity conditions. Error bars show 95% confidence intervals.

Figure 4-10 uses the same data sets and analysis as those in figure 4-9, except that the change in standard deviation is calculated from start to end, as opposed to the change in average value. This was done to analyze if the adverse environments affected the repeatability of the sensor, as opposed to the average reading. The figure has the same takeaways as figure 4-9; all changes in standard deviation fall within the error bars of the control tests, indicating that there is no significant change in the repeatability of the sensor when adverse environmental conditions are added. This further supports the same conclusions drawn from figure 4-9, that the levels of coal dust and moisture seen in a coal mine do not affect the radar sensor's ability to detect a static target. Further, several of the 95% confidence intervals cross zero, which indicates that there is no significant change in standard deviation from the start to end data sets at all. This implies that even without comparing to the control

data set, the change in standard deviation is negligible.

Again, this is limited by the size of the error bars. In this figure, the maximum possible change in standard deviation is approximately 0.7cm. This data implies that the addition of adverse environmental conditions could potentially cause an increase of 7mm in the standard deviation of the sensor readings, a slight reduction in sensor repeatability. Nonetheless, as before, this is only a small reduction in performance and is within an acceptable range for the purposes of obstacle avoidance.

4.4 Summary

A containted test setup was designed and assembled to create controlled environments mimicking the adverse conditions of a coal mine. The selected humidity sensors were shown to be well calibrated and accurate within their rated levels. The chosen dust sensors were correlated with video frame data to extrapolate beyond the upper dust concentration limit of the dust sensors. This correlation provided a method to calculate the airborne dust concentration using only video data.

The Walabot UWB radar sensor readings with and without adverse conditions present were compared to determine how the adverse conditions affected the sensor. Experimental data showed that when the sensor was detecting a static target, the sensor readings changed by less than 1cm within 95% confidence intervals, and the detected changes were comparable to those of the control tests performed without dust or moisture. This indicates that the Walabot sensor accuracy is indeed robust to the conditions of dust and humidity in a coal mine, and any affects caused by the adverse conditions are negligible. Further, the same results were found for sensor repeatability, indicating the sensor retains similar accuracy and repeatability when adverse conditions are present.

Chapter 5

Dynamic Target Detection in High Dust, Humidity

In this chapter, the experiments of chapter 4 were expanded to detect a dynamic target. The goal of these tests was to ensure that the sensor is still capable of reliably detecting a target in motion, despite adverse conditions. The same target used before, the orange sphere, was attached to a string to create a pendulum inside the controlled test environment. This chapter aims to experimentally demonstrate that the Walabot sensor is capable of detecting a dynamic target through the dust and humidity levels typically seen in a coal mine.

5.1 Experimental Design and Goals

The Walabot sensor was also tested with a dynamic target, as the sensor must be capable of detecting moving objects. With the static target testing, many data points were collected and averaged for data analysis, however, in a real world scenario the sensor must be able to quickly and accurately detect objects in motion to be able to avoid a collision. While the data collected in chapter 4 demonstrates that the radio waves are minimally scattered or reflected by the conditions present in the test environment, this may be simply because the average value over 50 data points was enough to reject any outliers caused by dust or moisture scattering. However, in a

dynamic scenario, each data point will be analyzed individually. Should the data collected from the sensor remain accurate and repeatable in adverse conditions, as in the previous two chapters, this will strengthen the claim that radio waves in the Walabot frequency range are minimally affected by dust and moisture. Further, it will also support the main goal of the study, that UWB radar is a robust solution for obstacle detection in harsh, real-world environments and scenarios.

As such, the tests in this chapter were designed to validate that the sensor can detect moving targets through the adverse environmental conditions present in a coal mine. The same acrylic box described in chapter 3 was used for all tests in this chapter, with the same mounting brackets for the radar sensor, the same fans, and the same sensors. The only change is that for these tests the spherical orange target was placed on a pendulum, as opposed to being mounted on a stationary peg. The target was attached to the roof of the test setup with fishing line so that it could swing freely from side to side. Magnets were placed inside the hollow target, such that when the target was pressed against the edge of the acrylic placing another magnet on the outside of the box would hold it in place. This allowed the target to be released externally without opening the test environment and breaking the seal, simply by removing the external magnet.

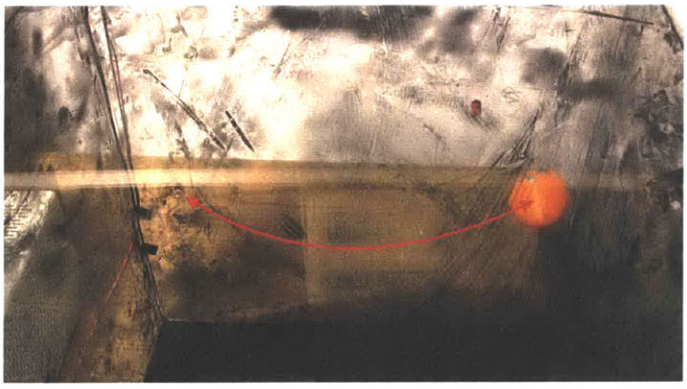

Figure 5-1: Orange spherical target acting as a pendulum, attached to the top of the test box with fishing line

Figure 5-1 shows a still image of the pendulum in the middle of a swinging motion during a coal dust test, with the motion of the pendulum illustrated in the red arrow. The pendulum is swinging along the y axis of the radar sensor, as illustrated in Figure

5-2.

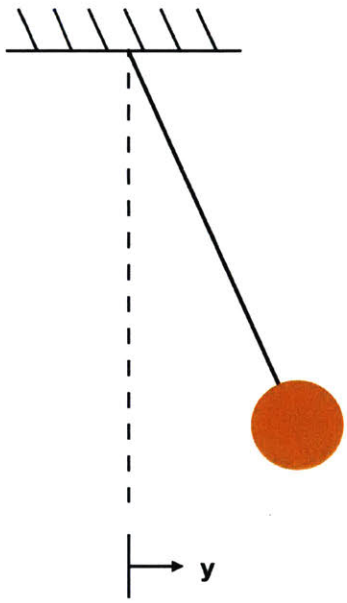

Figure 5-2: Target pendulum motion with y axis definition shown

Chapters 3, 4, and 6 all illustrate that the radar sensor has similar levels of accuracy and repeatability along all three axes in all tested scenarios. As such, in this chapter only the data from the y axis is analyzed as this is the most relevant data relative to the motion of the pendulum. The data along this axis will be used to represent the performance of the radar sensor as a whole. The collected data from the radar sensor in adverse conditions will be compared to the predicted pendulum motion, which can be characterized through the pendulum differential equations.

5.2 Pendulum Simulation

To develop a baseline for all data sets, the predicted motion of the pendulum target was calculated. To do so, first the free body diagram of a pendulum was analyzed. Figure 5-3 demonstrates the free body diagram for the target pendulum, only considering the forces acting on the pendulum perpendicular to the string.

In Figure 5-3, L is the length from the point of rotation to the center of the mass,

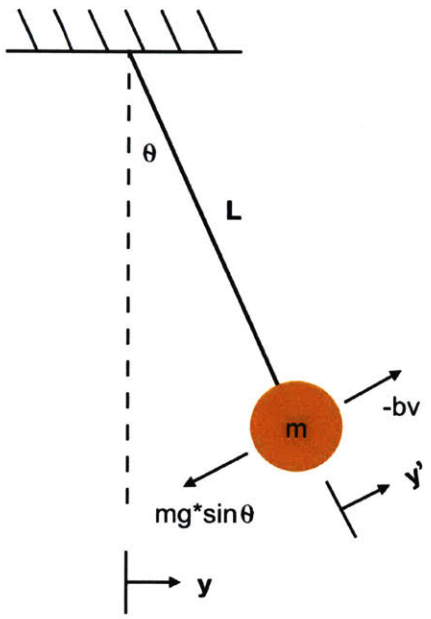

Figure 5-3: Target pendulum motion free body diagram

θ is the angle between the fishing line and the centerline of rotation, m is the mass of the target, g is the acceleration due to gravity, b is the damping coefficient, and v is the velocity of the mass. In all calculations for the predicted pendulum motion, a few assumptions are made. It is assumed the fishing line attaching the target to the box does not stretch, compress, or bend, and that the fishing line mass is negligible. Also, the assumption is made that the pendulum swings perfectly in plane, and thus oscillates purely in 2D.

By balancing the forces in the y' axis, we can derive a differential equation for the motion of the target, as a function of θ.

$$F = ma$$

$$ma = -mg\sin\theta - bv \tag{5.1}$$

Since we know the y' axis will perfectly sweep out the circle defined by radius L, we can treat the arc length as the "position" of the target. By differentiating the arc

length formula, we can determine the velocity and acceleration of the target.

$$arc = L\theta$$

$$v = L\frac{d\theta}{dt} \tag{5.2}$$

$$a = L\frac{d^2\theta}{dt^2} \tag{5.3}$$

Plugging equations (5.2) and (5.3) into equation (5.1), we get a differential equation with only θ and constants.

$$m(L\frac{d^2\theta}{dt^2}) = -mg\sin\theta - b(L\frac{d\theta}{dt})$$

$$\frac{d^2\theta}{dt^2} + \frac{b}{m}\frac{d\theta}{dt} + \frac{g}{L}\sin\theta = 0 \tag{5.4}$$

Equation (5.4) is the central differential equation that governs the system. Length L was measured with digital calipers to be 0.2460m, mass m was measured with a precision digital scale as 22.7217g, and g was assumed to be constant at 9.8067 m/s^2. Initially, a filler value of 0.01 was used for the damping coefficient b, and a more precise value was determined after collecting test data, described later.

Using these constant values, equation (5.4) was solved numerically in MATLAB using function ode45. The code used can be found in Appendix C. After calculating theta values over time, these values were then converted to y values using the following formula based on the geometry of Figure 5-3:

$$y = L\sin\theta$$

This resulted in the predicted y values over time. Next, to determine the damping coefficient, the collected control data shown in Figure 5-4 was used to fit the predicted data. The peak occurring right after 37 seconds was used, as the data had no outliers

on this peak. The maximum y values recorded from each trial at this point were averaged, and the predicted MATLAB solution was then forced to go through this point. The resulting damping coefficient, b, was 0.000497. The equation for θ, equation (5.4), was then re-solved with this new b value and converted to y values once more, resulting in the appropriate predicted y values for the motion of the pendulum used in the experiments this chapter.

These predicted y values were used as a relative baseline for all tests in section 5.3, and are plotted in gray in all remaining figures in this chapter. If the recorded sensor data in the y axis closely matches the predicted data, this indicates that the sensor is capable of tracking the object despite the adverse environmental conditions.

5.3 Radar Sensor Data

For the tests in this chapter, the radar sensor was programmed to operate in a dynamic mode, applying a moving target identification (MTI) filter. This filter is a temporal high filter, meaning that during signal processing the less a detected object moves from frame to frame, the more this reading is attenuated. This essentially means that the sensor will ignore any static object, and only record moving targets. The slower a target is moving, the more difficult it will be to detect in this mode. The threshold for this detection will depend on the speed of the target, how radar reflective it is, and how much noise is present in the signal. This filter is useful for the purposes of this test, to ensure any static targets are ignored and only the moving target swinging on the pendulum is recorded.

The same arena as that defined in chapter 4 was utilized, reaching 1m in length and extending $\pm$ 25 degrees in both the horizontal and vertical axes.

The control tests are defined as follows; data recording starts, then after 10 seconds to allow for ample time for the sensor initialization the fans are turned on, and then five seconds later the magnets holding the pendulum in place are released. After one minute, the sensor is turned off and the recording is ended. The data collected from these tests was termed the 'control' data, and was used as a baseline for this chapter.

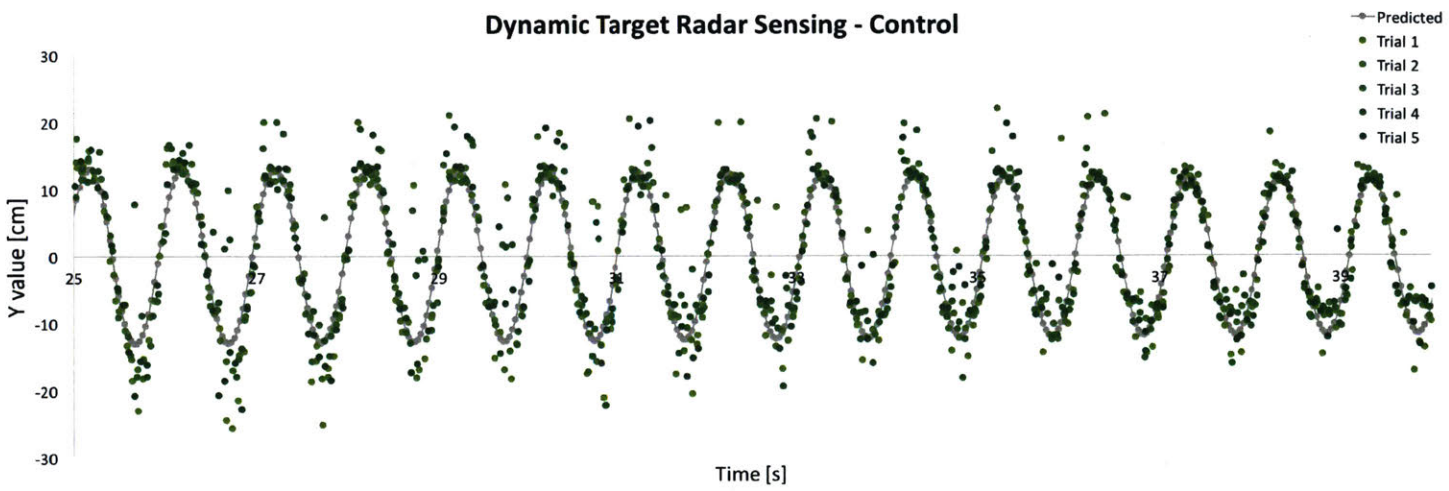

Figure 5-4: Results of dynamic target radar sensor testing in control tests. The predicted pendulum model is the solid line.

As shown in Figure 5-4, the test data has a large number of outliers, particularly at the peaks and valleys of the predicted path, where the test data does not match the predicted data. This is likely due to the low velocity of the target around these points; the radar sensor is operating in a mode that ignores stationary targets, so when the target velocity drops down to zero as it changes direction, the MTI filter described above will attenuate the target readings until it becomes indistinguishable from sensor noise. This will cause the erroneous readings seen in Figure 5-4. To illustrate that this is primarily a signal processing issue, and not a sensor capability issue, the data points near the peaks and valleys were removed from the graph in Figure 5-6.

To remove these outliers, the differential equation data from section 5.2 was utilized to determine when the absolute value of the velocity of the target falls below a threshold value. As Figure 5-4 illustrates, the outliers occur around the peaks of the predicted model, particularly when the predicted model goes above 10cm or below -10cm. From the differential equation data in section 5.2, the predicted model velocity drops below 0.5 m/s when the target y value first goes above 10cm or below -10cm. As such, 0.5 m/s was used as the threshold velocity.

Next this threshold value was used to remove the outlier points. First, the time

intervals in the predicted model with velocities below this threshold were determined. These intervals indicate when the target is expected to have a velocity below 0.5 m/s. Then, any experimental data points with a timestamp falling inside these intervals was removed from the graph to filter out unwanted outlier points.

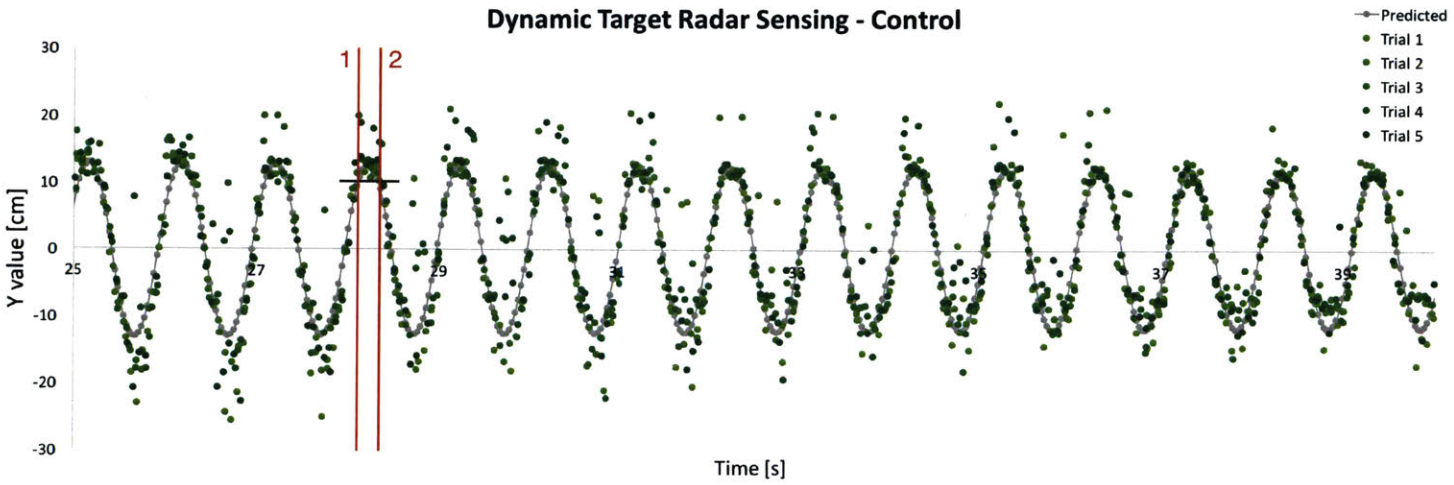

Figure 5-5: Illustration of the thresholds for the removal of low velocity points

For example, in Figure 5-5 this process is illustrated for the peak occurring at approximately 28 seconds. The horizontal black line indicates when the predicted model goes above 10cm, and the red vertical lines indicate the time interval where the predicted model velocity is below 0.5 m/s. The red line labeled 1 indicates when the velocity drops below 0.5 m/s, and line 2 indicates when the velocity increases past 0.5 m/s again. Any experimental data points, shown in green, that fall between the two red lines are removed, as the MTI filtering described above becomes unreliable in this low-velocity zone. The same process is repeated for each peak and valley, and the resulting data points are plotted in Figure 5-6.

In Figure 5-6, it is clear that for all data points taken when the target has a sufficiently high velocity, the sensor is able to reliably track the moving target, with test data that closely matches the predicted data. This demonstrates that the outlier problem in Figure 5-4 is indeed a signal processing issue, and not an inability of the sensor to track the target. Only a few outliers remain and they are spread out

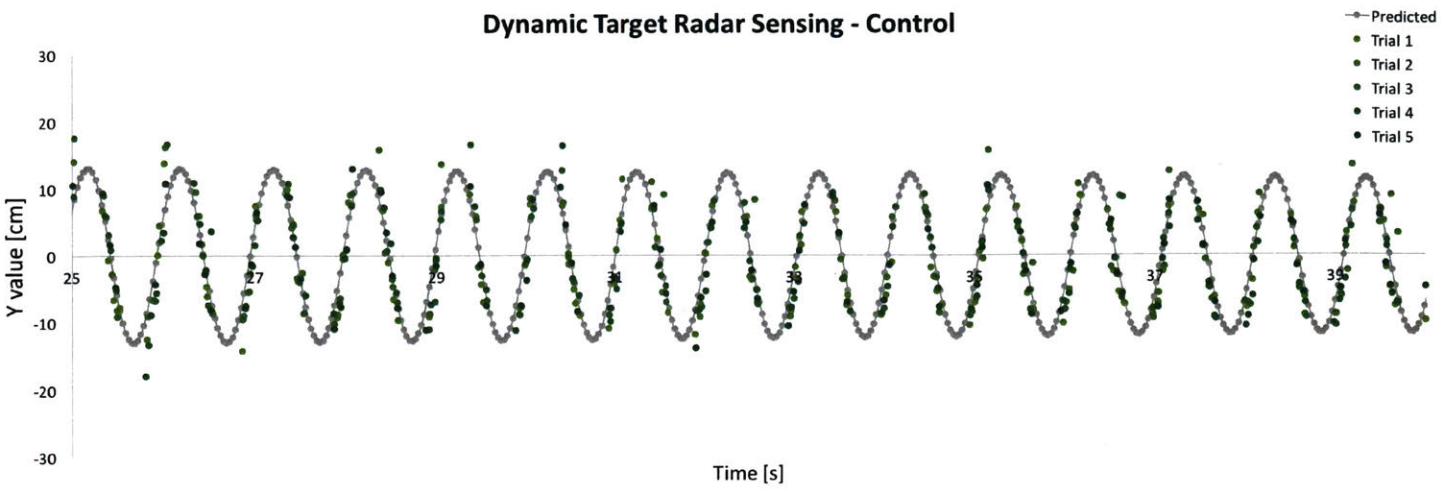

Figure 5-6: Results of dynamic target radar sensor testing in control conditions with low velocity points removed

amongst all five trials, indicating strong performance from the sensor. These few outliers can be attributed to sensor noise. Otherwise, the collected test data, from all trials, stays very close to the predicted data curve, implying that the sensor is able to track a moving target with strong accuracy and repeatability. This figure validates the predicted model as a baseline for the tests performed in adverse conditions.

It should be noted that while this is acceptable for the purposes of this study, as we are primarily concerned with characterizing sensor performance in a controlled test scenario, in typical use on a drone the sensor must be capable of detecting both static and dynamic targets. While the drone is in motion, dynamic target analysis is sufficient as all potential obstacles will be moving relative to the drone. However, while the drone is hovering, it must detect nearby obstacles so that it does not collide with an obstacle when it begins to move. As such, for implementation on a fully operational drone, a slightly more complex signal processing algorithm would be necessary to combine both static and dynamic target detection processes, depending on the drone's velocity.

Next, the same test process was utilized for the coal dust testing, except that 32g of coal dust are added into the box prior to testing. Then, when the fans are turned on, the dust is kicked up into the air for the duration of the test. The only dust

level tested in this experiment is the maximum dust level, with 32g in the test setup, reaching approximately 4.27 mg/m^3 of airborne dust, as described in section 4.2.

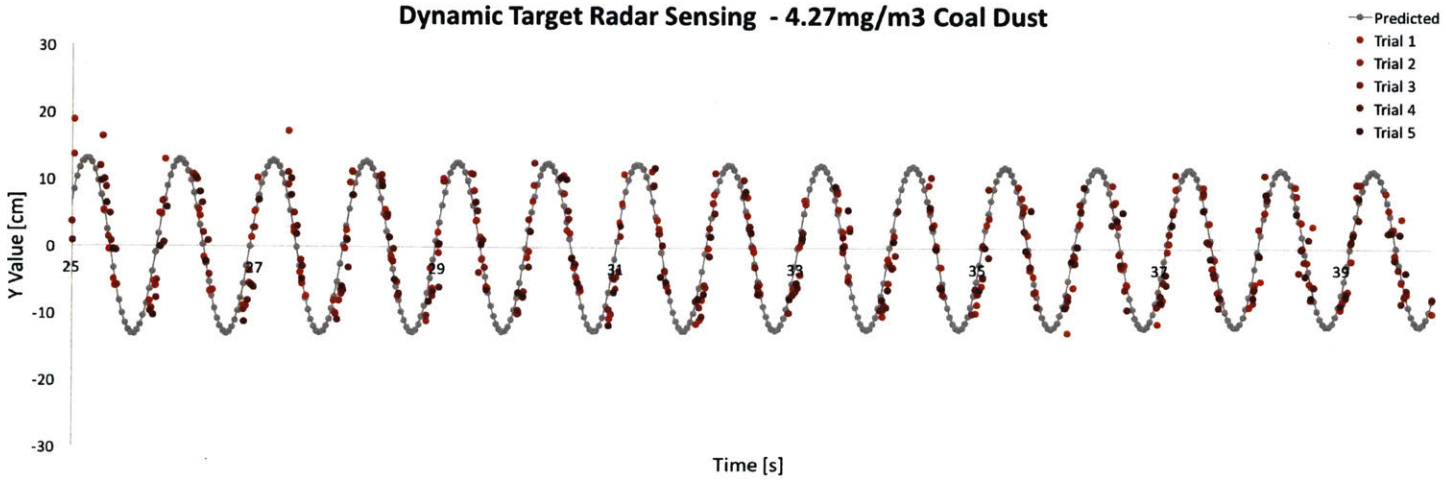

Figure 5-7: Results of dynamic target radar sensor testing with 4.27 mg/m^3 of coal dust, with low velocity points removed

In Figure 5-7, the low velocity points were again removed using the same process described for Figure 5-2. The test data again follows the predicted data closely in all five trials, demonstrating that the sensor retains strong accuracy and repeatability despite the presence of the coal dust.

The third and final step was to collect humidity data. For these tests, prior to starting the test, water is sprayed into the box and the fans are turned on to rapidly increase the humidity in the box. Once both humidity sensors read 99% RH, the sensor began to record data. After waiting 15 seconds to ensure this humidity data is synchronized to the control test data, the pendulum is released. One minute later, the sensor was turned off.

Figure 5-8 illustrates the collected humidity testing data, again with low velocity points removed. As with the coal dust testing, the test data again closely follows the predicted data in all five trials, indicating that the radar sensor still maintains strong accuracy and repeatability despite the high levels of humidity.

As demonstrated in Figures 5-7 and 5-8, the sensor data collected in the environmental conditions of a coal mine follow the predicted data quite closely, with the exception of a small number of outliers. These two figures show that the accuracy

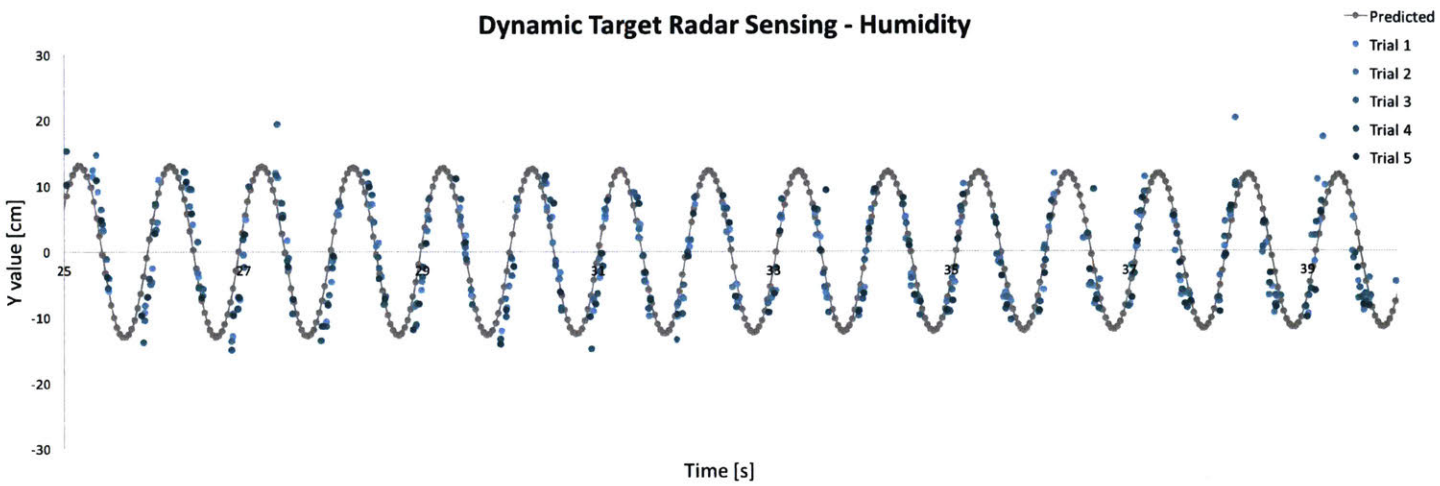

Figure 5-8: Results of dynamic target radar sensor testing with 99% relative humidity, with low velocity points removed

and repeatability of the sensor do not depend on a static target with ample time to make multiple measurements and average those together. This dynamic target data illustrates that each individual data point has a high level of accuracy and repeatability, as each data point stays close to the predicted curve and there is no noticeable discrepancy from trial to trial. This data, as the data in chapter 4 does, continues to support the hypothesis that electromagnetic waves in the range of 3.3 - 10.3 GHz are minimally scattered or reflected by airborne dust and moisture particles. These strong results when following a target in motion further support the initial claim that UWB radar is a strong candidate for use on a drone in adverse environments, particularly in coal mines.

5.4 Summary

The Walabot sensor was tested in similar experiments to those described in chapter 4, except using a dynamic target as opposed to a static one. The same orange sphere used previously was attached to a string to create a pendulum. The differential equation for the motion of this pendulum was solved to create a predicted model for the motion of the target. This predicted model was then compared to sensor readings taken in clear, dusty, and humid conditions. The sensor recorded many

outliers when the target slowed down at the edges of the pendulum motion, as the MTI filter used attenuated the readings from slow moving targets. Nonetheless, in all three conditions, the sensor readings closely matched the predicted model once the low-velocity points were removed. This indicates that the Walabot sensor is indeed capable of detecting moving targets well even in adverse conditions.

Chapter 6

Anomalous Propagation in Radar

In this chapter, the Walabot UWB Radar sensor was experimentally tested to ensure that no anomalous propagation of the radio waves occurs. Some environmental conditions can cause errors in long-range, conventional radar systems, where the radio waves do no propagate as expected. This chapter aims to demonstrate that drone propeller airflow will not cause a similar error in propagation in short range UWB systems.

6.1 Principles of Anomalous Propagation

Anomalous propagation (AP) is the term used to describe when atmospheric conditions cause radio waves to propagate in unexpected ways. In conventional radar systems, this is typically caused by temperature inversions or strong moisture gradients in the atmosphere [28]. This is primarily due to the fact that variations in temperature or moisture will affect the resulting refractive index of air, as refractive index tends to vary with the density of the medium [28]. This change in the refractive index of air will alter the path of the radio waves, as described in chapter 2, resulting in skewed readings from the radar.

There are several types of anomalous propagation, as illustrated in Figure 6-1 [29]. In the figure, α represents the small tilt angle of the emitted radar beam, relative to the horizontal plane of the Earth's surface. The differing propagation regimes shown

are subrefraction (SUB), normal refraction (NORM), superrefraction (SUPR), and ducting (DUCT). Ducting is a special case of superrefraction where the radar beam is trapped and forced to continuously reflect off the ground. These definitions are commonly used with conventional, long-range radar systems.

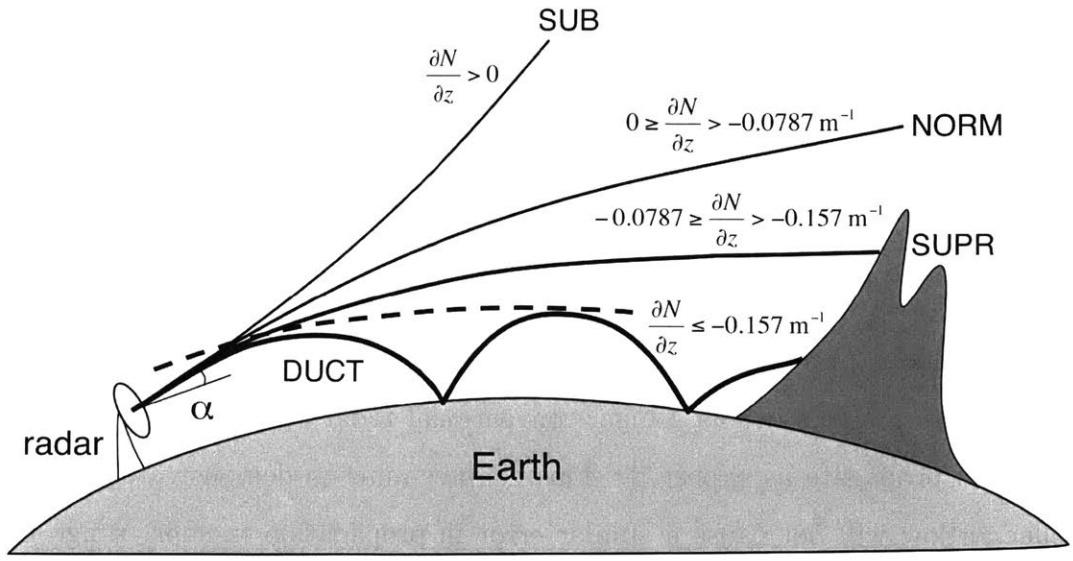

Figure 6-1: Propagation regimes of a ground-based radar beam [29]

In Figure 6-1, the propagation regimes are labeled based on the refractivity gradient with respect to height, $\frac{\partial N}{\partial z}$. N is the refractivity of the air, and z is the height relative to the Earth's surface. This number indicates the rate at which the refractivity of air is varying as height increases. Refractivity is used in anomalous propagation studies instead of the the refractive index, as the variations in refractive index are very small, on the order of magnitude of 1×10^{-6} [28]. The equation relating the two is:

$$N = (n - 1) \times 10^6$$

Where N is the refractivity, and n is the refractive index.

6.1.1 Anomalous Propagation from Drone Propeller Airflow

For this study, our radar sensor must be able to maintain strong performance when mounted onto a drone, without anomalous propagation affecting the sensor readings. The primary change when using the radar sensor on a drone is the presence of the propeller air flow. Otherwise, the drone can be treated simply a vehicle for moving the sensor. Similar to the atmospheric changes discussed above, the propeller air flow will result in varying air pressures and air densities, which will affect the index of refraction of the air near the propellers.

This effect is expected to be negligible in the context of drone propellers, though it has not been directly tested before. In conventional radar systems, a sensor range on the order of tens of kilometers is common, meaning even small changes in the refractive index, n, can result in large errors as the radio wave propagates for many kilometers. For a drone, however, the characteristic length is defined by the length of the propeller. This is because the propeller length defines the diameter of the airflow column created when the propeller spins; this is the distance through which the radio waves must travel where the refractive index has changed due to the induced airflow. The Erle-Copter drone propellers are 24cm long, approximately 5 orders of magnitude shorter than the sensor ranges of conventional radar systems. Due to this relatively short distance and the small variation in refractive index caused by typical environmental conditions, it is expected that the potential for anomalous propagation due to drone propeller airflow is negligible.

It must still be verified experimentally that these effects are negligible on a drone. The refractive index of air is an empirically determined value, and will vary both with the medium and the frequency of the wave being transmitted. As such, we must ensure that the particular frequencies used by the Walabot sensor and the pressure gradient caused by the Erle-Copter will not result in dramatically larger variations in the refractive index of air. Although it is likely the change in refractive index from propeller airflow will have a similar order of magnitude as that of typical atmospheric variations, it is best to validate this assumption through experimental data, since

the index of refraction must be determined empirically. This chapter endeavors to provide the experimental data and analysis that demonstrate anomalous propagation is not a concern for the use of the Walabot UWB radar on a drone.

6.2 Experimental Design and Goals

To illustrate that anomalous propagation will not occur when mounting UWB radar sensors on a drone, the Walabot sensor was mounted onto a stationary drone and tested with and without the propellers active. If the propeller airflow, and the resulting air pressure gradients, alter the propagation of the radio waves from the radar sensor, this will skew the sensor readings when detecting a target. If not, the sensor readings will remain consistent whether or not the propellers are on.

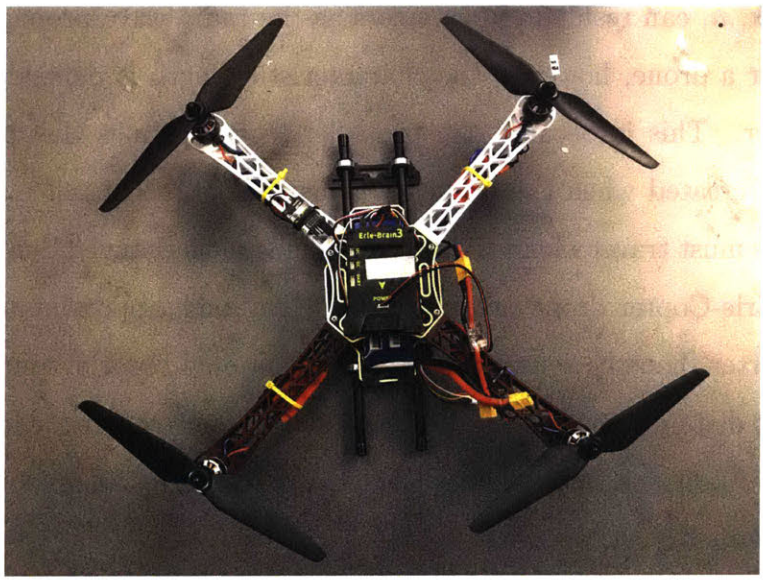

Figure 6-2: Assembled Erle-Copter drone

The Erle-Copter drone, shown in Figure 6-2 was selected for use in this testing. This drone is a modular, low-cost, and developer friendly option. It has various mounting points for additional modules or sensors, either from Erle Robotics or third party vendors. These were used to mount the Walabot sensor underneath the drone, so that the effect of the propeller airflow could be analyzed. The sensor was programmed using the static sensor mode, described in section 3.2, with an arena defined

to reach 5m with a field of view extending ± 25 degrees in both the horizontal and vertical directions. This is the same programmed setup used for all characterizing tests in chapter 3.

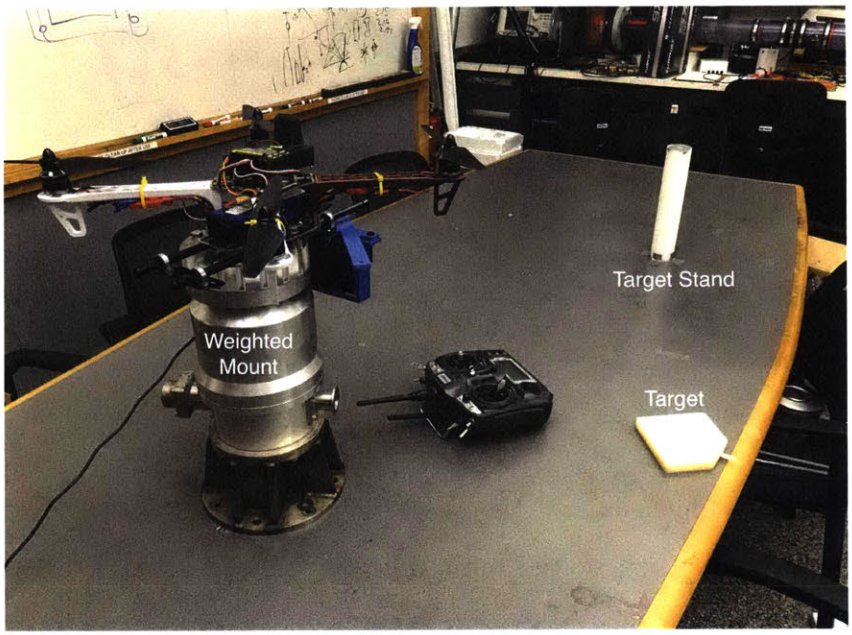

Figure 6-3: Anomalous propagation drone testing setup. Target stand approximately 1.5m away.

The testing setup used for all tests in this chapter is shown in Figure 6-3. To ensure the drone remained stationary throughout testing, it was bolted down onto a heavy weighted mount. The drone must remain motionless during the testing despite the thrust from the propellers, so that any detected changes from the radar sensor are the result of the propeller airflow and not the motion of the drone. This mount ensures the drone doesn't move or lift off, and it also props the drone up to reduce the interference of ground effects on the propeller airflow. The target stand and the plastic target used in this testing are also pictured. The target stand is approximately 1.5m away from the drone at the same height, and provides a repeatable mounting location for the target.

A simple blue 3D printed plastic mount was designed to attach the Walabot sensor to the Erle-Copter. This mount, shown in Figure 6-4, has two pieces. The top piece bolts directly onto available mounting points on the drone. The bottom piece is U

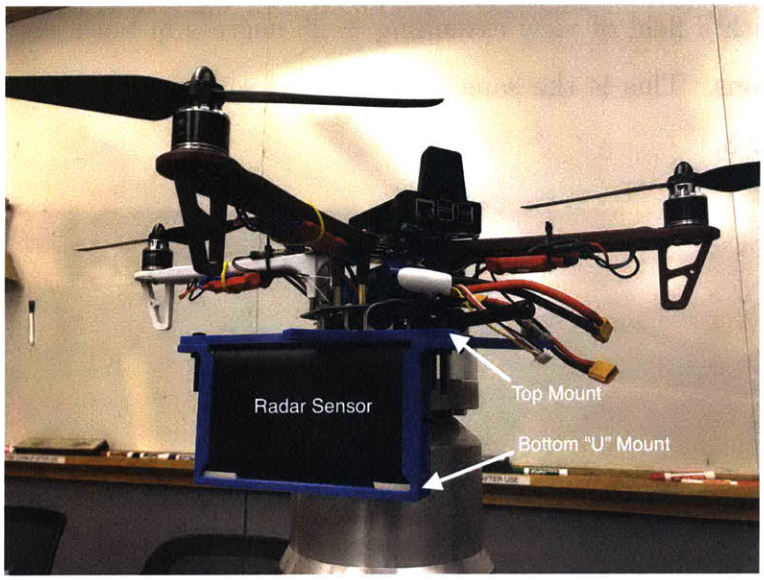

Figure 6-4: Walabot radar sensor mounted onto the Erle-Copter drone

shaped and fits the dimensions of the Walabot sensor, such that the sensor can be slotted into the U and then bolted onto the top piece to firmly hold the sensor in place.

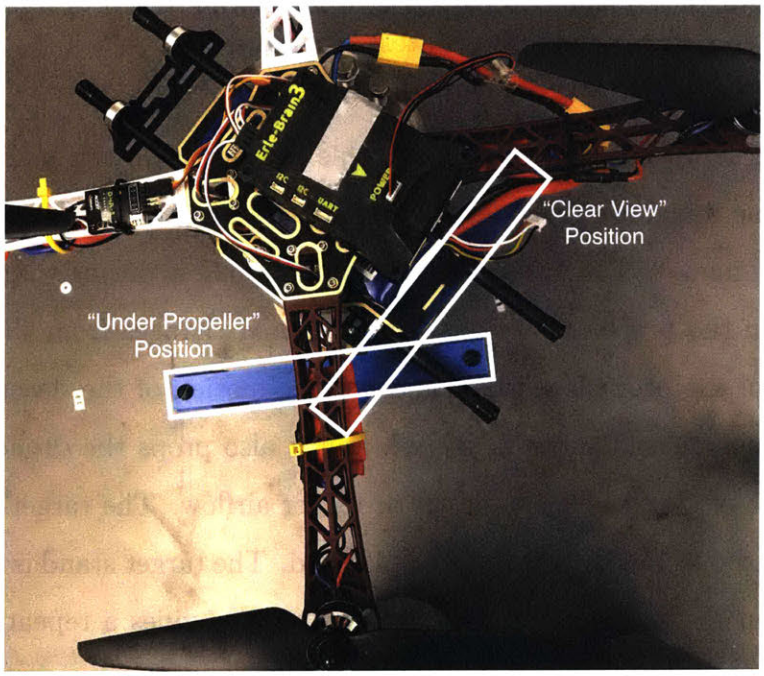

Figure 6-5: Overhead image illustrating "clear view" and "under propeller" radar sensor mounting locations

The top mount was designed to have two mounting points for the radar sensor.

One position is centered in between the arms of the drone such that the sensor has a clear view. The second is directly underneath one of the arms such that the sensor looks directly underneath the propeller, forcing the radio waves to propagate directly through the propeller airflow. These two mounting positions are shown in Figure 6-5.

6.3 Radar Sensor Data

To characterize the effect of the propellers on the radar sensor reading, a testing method similar to that in chapter 4 was used. First, the radar sensor was initialized to the empty table with the target stand. Then the target was placed on the stand and "start" data was recorded for 30 seconds. The drone was then powered on, and the throttle was placed at half power. After 30 more seconds of "end" data were recorded with the propellers on, the sensor and the drone were powered down.

This test was performed with the sensor mounted in both mounting positions, first in between the propellers with a clear view, and then directly underneath the propeller. In both cases, the drone was oriented such that the sensor was facing the same direction for all tests, parallel to the table it was mounted on. The clear view test was performed as a control test to characterize any potential sources of error other than the air gradients caused by propeller airflow, such as vibrations induced by the propellers. In this way, the only change between the two test cases is the presence of the propeller's airflow in front of the radar sensor, so any changes caused by the variable air density can be isolated by comparing these two data sets.

An average change in sensor readings from start to end data sets was calculated for all three axes, following the same process described in section 4.3. These calculated values are shown in Figure 6-6, with 95% confidence intervals represented by the error bars. This figure illustrates once again that there is no negligible change between the two data sets. Along all three axes, the error bars from the two mounting positions overlap, indicating that there is no significant change between the two data sets. As discussed in section 6.1, this is likely because the variation in the index of refraction of the air beneath the propellers is small, and the characteristic length of the propeller

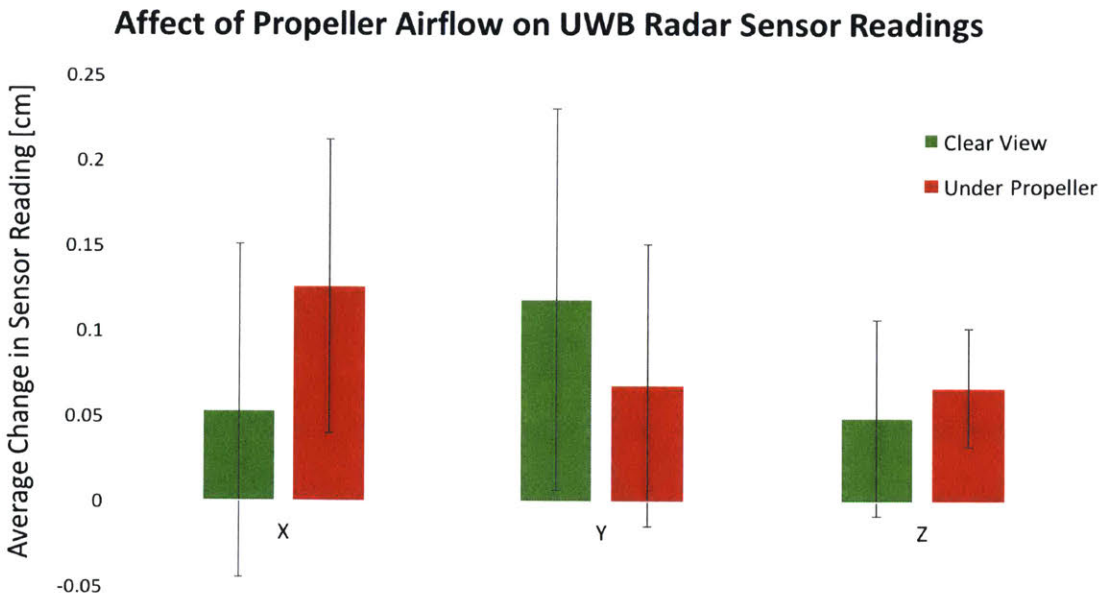

Figure 6-6: Results of static target radar sensor testing in anomalous propagation conditions. Error bars show 95% confidence intervals.

is extremely small relative to those seen by conventional radar sensors. As a result, the variation it causes in sensor performance is negligible.

The average changes in sensor readings are on the order of 1mm, and no error bar exceeds 2.5mm. These values are comparable to the levels of repeatability and accuracy seen in chapter 3, when characterizing the radar sensor performance in ideal conditions. Also, this maximum error of 2.5mm is less than 0.2% of the distance to the target, only a small fraction. This clearly supports the claim that mounting the radar sensor on the drone will have no noticeable effect on sensor performance. Even if there is some discrepancy caused by the propeller airflow that is masked by the size of the error bars, the largest possible discrepancy within 95% confidence intervals is approximately 2.5mm. This small variation is well within acceptable tolerance levels for the purposes of obstacle detection and avoidance.

6.4 Summary

In conventional long-range radar systems, anomalous propagation is a well understood problem that can cause erroneous readings. However, for short range radar through propeller airflow, the affects of anomalous propagation have not been tested. To ensure that drone propellers and their associated airflow won't cause anomalous propagation of radio waves, the Walabot sensor was mounted onto an Erle-Copter drone and tested with the propellers spinning. In one mounting position, the UWB radar sensor was directly underneath the propeller, forcing the radio waves to travel through the propeller airflow. In the second, the sensor had a clear view. In both mounting positions, the sensor was able to repeatably and accurately detect a static target. There were no observed differences in the sensor readings taken from the two mounting positions. This indicates that propeller airflow has a negligible affect, if any, on the propagation of radio waves, and anomalous propagation concerns can be neglected in this scenario.

Chapter 7

Conclusion and Recommendations

In this study, UWB radar technology is analyzed and tested for use on an inspection drone in underground coal mines. The sensor used to exemplify UWB radar technology is the Walabot Pro sensor. This sensor was tested both in clear conditions and the adverse conditions expected in a coal mine, particularly high humidity and dust concentration levels. The sensor was tested in environments with up to 99% relative humidity and 4 mg/m^3 of coal dust present.

In clear conditions, the sensor performance was very strong. The Walabot sensor was able to detect a stationary target with an accuracy on the order of centimeters up to a tested distance of 4m. Further, a resolution of 5mm was consistently achieved, with repeatability on the order of microns. Though the sensor has a relatively low accuracy, the resolution and repeatability are incredibly strong.

In adverse conditions, the sensor performance remained adequately strong, both when measuring a stationary and a dynamic target. In both situations, the sensor readings exhibited small variations when measurements in clear and adverse conditions were compared. The change in readings was less than 1cm, indicating that the adverse conditions have a negligible effect on sensor performance. This implies that sensor accuracy will drop by 1cm at worst when used in adverse conditions typically present in a coal mine. This drop is within acceptable levels for the inspection drone to be capable of avoiding obstacles in its path.

The Walabot sensor was also mounted beneath a drone to test whether or not the

drone propellers might affect sensor performance through anomalous propagation. As with the adverse condition tests, drone propellers and their associated airflows were found to have a negligible effect on sensor performance. There were no observed differences between sensor readings taken with the propellers off and with the propellers on. This implies that mounting a UWB radar sensor on a drone will not affect its performance in any way.

These experimental results strengthen the support for UWB radar as a robust sensor for use in coal mine environments. UWB radar technology is clearly capable of detecting targets and obstacles, even through the adverse conditions present in an underground coal mine. I believe UWB radar is a great candidate for coal mine use, particularly for an inspection drone, and recommend further tests be performed in a coal mine. As automation continues to be explored and applied to coal mines, UWB radar is a useful tool to support and strengthen this trend.

Further drone testing and signal processing is recommended for future work. The UWB sensor was tested only on a stationary drone, and it must be capable of operating on a flying drone without any drop in performance. Also, only simple filtering methods provided in Walabot sample code were utilized in this study; there is an opportunity for more complex signal processing algorithms to obtain more useful data from a UWB radar sensor. For example, this algorithm could integrate IMU data to help detect both stationary and dynamic targets simultaneously, characterize whether a detected target is a wall, machine, human, or any other potential obstacle, and reduce outliers, among other possible benefits. There is a huge potential for increasing the utility of this sensor through signal processing that has not been explored.

Appendix A

Uncertainty Calculations

For all uncertainty calculations performed in this study, the equations below were used. These characterize how the 95% confidence interval was calculated for the average value of a set of measurements. These calculations assume the set of measurements taken are samples of an independent variable that follows a Gaussian probability distribution.

Assume a set of N measurements $(x_1, x_2, x_3, ...x_N)$ for these equations.

First the mean, x_{avg}, was calculated by taking the sum of all measurements and dividing by the number of measurements:

$$x_{avg} = \frac{\sum_{i=1}^{N} x_i}{N}$$

Next the standard deviation of the data set, σ, was calculated:

$$\sigma = \sqrt{\frac{\sum_{i=1}^{N}(x_i - x_{avg})^2}{N-1}}$$

Then the standard deviation of the mean, S, was calculated:

$$S = \frac{\sigma}{\sqrt{N}}$$

Finally, the 95% uncertainty on the mean value, u, was calculated using the t-factor. This factor is described below:

$$u = tS$$

The value t is known as the t-factor. This factor is determined by the degrees of freedom, v, of the data set. For this case, a simple mean calculation, v is simply $N - 1$. Note that t will also vary with the desired confidence interval. If v is greater than 30, the t-factor will be 2 for 95% confidence [30]. For values of v 30 or below, indicating a small sample size, the t-factor will increase and can be determined from a t-factor table [30]. The table for 95% confidence values is shown below.

Now that the uncertainty is known, the average value of the set of measurements can be written as:

$$x_{avg} \pm u$$

This indicates the range within which we are 95% confident the true mean of the measured variable will be. This method was used for data analysis in all chapters.

v	t	v	t	v	t
1	12.706	11	2.201	21	2.080
2	4.303	12	2.179	22	2.074
3	3.182	13	2.160	23	2.069
4	2.776	14	2.145	24	2.064
5	2.571	15	2.131	25	2.060
6	2.447	16	2.120	26	2.056
7	2.365	17	2.110	27	2.052
8	2.306	18	2.101	28	2.048
9	2.262	19	2.093	29	2.045
10	2.228	20	2.086	30	2.042

Table A.1: t-factor table for 95% confidence intervals [30]

Appendix B

Accessory Hardware Datasheets

This appendix has datasheets and information for the humidity sensor, dust sensor, and fans used inside the testing setup.

B.1 Humidity Sensor

The selected humidity sensor is the Honeywell HIH-4030 sensor. The two purchased sensors were factory calibrated, with the factory calibration data given below:

Sensor Number	Calibration Slope	Calculation Zero Offset
1	30.55 mV/%RH	0.858 V
2	30.61 mV/%RH	0.845 V

Table B.1: Table containing humidity sensor calibration values

With these calibration values, the relative humidity (RH) value can be calculated from the output voltage of the sensor, V_{out}:

$$\text{RH } [\%] = \frac{(V_{out} - \text{zero offset})}{\text{slope}}$$

The sensor datasheet is also shown below, on pages 87-93.

B.2 Dust Sensor

The selected dust sensor is the Sharp GP2Y1010AU0F Optical Dust Sensor. This sensor was purchased from DFRobot.com, along with a dust sensor adapter to simplify connecting to the dust sensor. The dust sensor adaptor has SKU DFR0280 on the DFRobot website.

The data sheet for this sensor is shown below, on pages 94-99.

B.3 Fan

The fans used inside the test setup were purchased from Amazon.com. They are manufactured by Yate Loon, with part number D50SH-12C. The dimensions are 50mm x 50mm x 20mm and they are powered with 12V DC, drawing 0.27A when powered on. The rated RPM is 6000, with an airflow of 19 CFM and 38dB of noise.

Honeywell

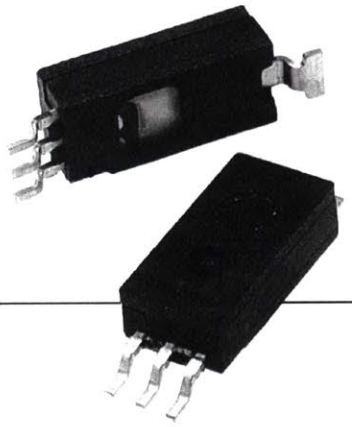

HIH-4030/31 Series

Humidity Sensors

DESCRIPTION

Honeywell has expanded our HIH Series to include an SMD (Surface Mount Device) product line: the new HIH 4030/4031. The HIH 4030/4031 complements our existing line of non-SMD humidity sensors. SMD packaging on tape and reel allows for use in high volume, automated pick and place manufacturing, eliminating lead misalignment to printed circuit board through-hole.

The HIH-4030/4031 Series Humidity Sensors are designed specifically for high volume OEM (Original Equipment Manufacturer) users.

Direct input to a controller or other device is made possible by this sensor's near linear voltage output. With a typical current draw of only 200 µA, the HIH-4030/4031 Series is often ideally suited for low drain, battery operated systems.

Tight sensor interchangeability reduces or eliminates OEM production calibration costs. Individual sensor calibration data is available.

The HIH-4030/4031 Series delivers instrumentation-quality RH (Relative Humidity) sensing performance in a competitively priced, solderable SMD.

The HIH-4030 is a covered integrated circuit humidity sensor. The HIH-4031 is a covered, condensation-resistant, integrated circuit humidity sensor that is factory-fitted with a hydrophobic filter allowing it to be used in condensing environments including industrial, medical and commercial applications.

The RH sensor uses a laser trimmed, thermoset polymer capacitive sensing element with on-chip integrated signal conditioning.

The sensing element's multilayer construction provides excellent resistance to most application hazards such as condensation, dust, dirt, oils and common environmental chemicals.

Sample packs are available. See order guide.

FEATURES

- Tape and reel packaging allows for use in high volume pick and place manufacturing (1,000 units per tape and reel)
- Molded thermoset plastic housing
- Near linear voltage output vs %RH
- Laser trimmed interchangeability
- Low power design
- Enhanced accuracy
- Fast response time
- Stable, low drift performance
- Chemically resistant

POTENTIAL APPLICATIONS

- Refrigeration equipment
- HVAC (Heating, Ventilation and Air Conditioning) equipment
- Medical equipment
- Drying
- Metrology
- Battery-powered systems
- OEM assemblies

HIH-4030/31 Series

TABLE 1. PERFORMANCE SPECIFICATIONS (At 5 Vdc supply and 25 °C [77 °F] unless otherwise noted.)

Parameter	Minimum	Typical	Maximum	Unit	Specific Note
Interchangeability (first order curve)	–	–	–	–	–
0% RH to 59% RH	-5	–	5	% RH	–
60% RH to 100% RH	-8	–	8	% RH	–
Accuracy (best fit straight line)	-3.5	–	+3.5	% RH	1
Hysterisis	–	3	–	% RH	–
Repeatability	–	±0.5	–	% RH	–
Settling time	–	–	70	ms	–
Response time (1/e in slow moving air)	–	5	–	s	–
Stability (at 50% RH in a year)	–	±1.2	–	% RH	2
Stability (at 50% RH in a year)	–	±0.5	–	% RH	3
Voltage supply	4	–	5.8	Vdc	4
Current supply	–	200	500	µA	–
Voltage output (1st order curve fit)	$V_{OUT}=(V_{SUPPLY})(0.0062(\text{sensor RH}) + 0.16)$, typical at 25 °C				
Temperature compensation	True RH = (Sensor RH)/(1.0546 – 0.00216T), T in °C				
Output voltage temp. coefficient at 50% RH, 5 V	–	-4	–	mV/°C	–
Operating temperature	-40[-40]	See Figure 1.	85[185]	°C[°F]	–
Operating humidity (HIH-4030)	0	See Figure 1.	100	% RH	5
Operating humidity (HIH-4031)	0	See Figure 1.	100	% RH	–
Storage temperature	-50[-58]	–	125[257]	°C[°F]	–
Storage humidity	See Figure 2.			% RH	5

Specific Notes:

1. Can only be achieved with the supplied slope and offset. For HIH-4030/31-003 catalog listings only.
2. Includes testing outside of recommended operating zone.
3. Includes testing for recommended operating zone only.
4. Device is calibrated at 5 Vdc and 25 °C.
5. Non-condensing environment. When liquid water falls on the humidity sensor die, output goes to a low rail condition indicating no humidity.

General Notes:

- Sensor is ratiometric to supply voltage.
- Extended exposure to ≥90% RH causes a reversible shift of 3% RH.
- Sensor is light sensitive. For best performance, shield sensor from bright light.

FACTORY CALIBRATION DATA

HIH-4030/31 Sensors may be ordered with a calibration and data printout. See Table 2 and the order guide on the back page.

TABLE 2. EXAMPLE DATA PRINTOUT

Model	HIH-4030-003
Channel	92
Wafer	030996M
MRP	337313
Calculated values at 5 V V_{OUT} at 0% RH V_{OUT} at 75.3% RH	 0.958 V 3.268 V
Linear output for 3.5% RH accuracy at 25 °C Zero offset Slope Sensor RH	 0.958 V 30.680 mV/%RH (V_{OUT} - zero offset)/slope (V_{OUT} - 0.958)/0.0307
Ratiometric response for 0% RH to 100% RH V_{OUT}	 V_{SUPPLY} (0.1915 to 0.8130)

FIGURE 1. OPERATING ENVIRONMENT (Non-condensing environment for HIH-4030 catalog listings only.)

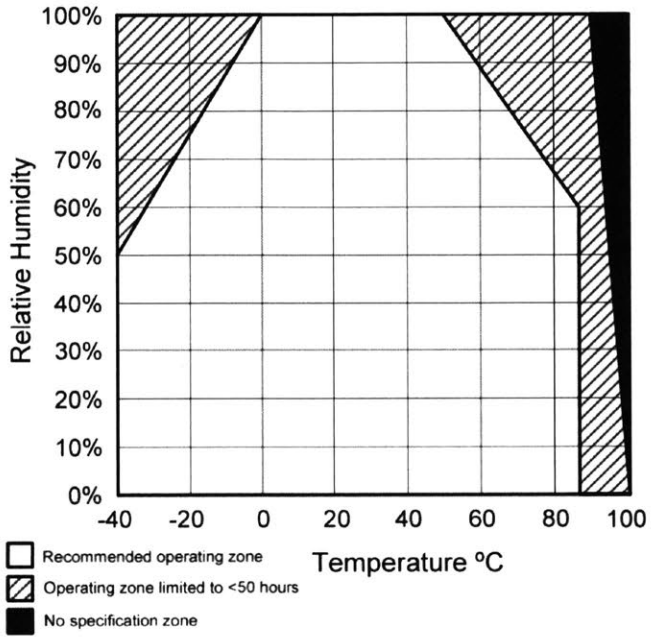

FIGURE 2. STORAGE ENVIRONMENT (Non-condensing environment for HIH-4030 catalog listings only.)

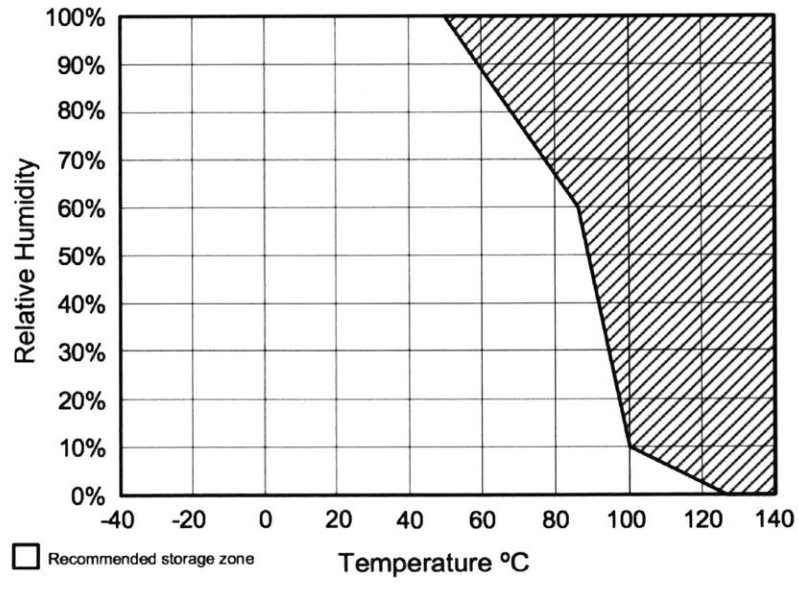

FIGURE 3. TYPICAL OUTPUT VOLTAGE VS RELATIVE HUMIDITY (At 25 °C and 5 V.)

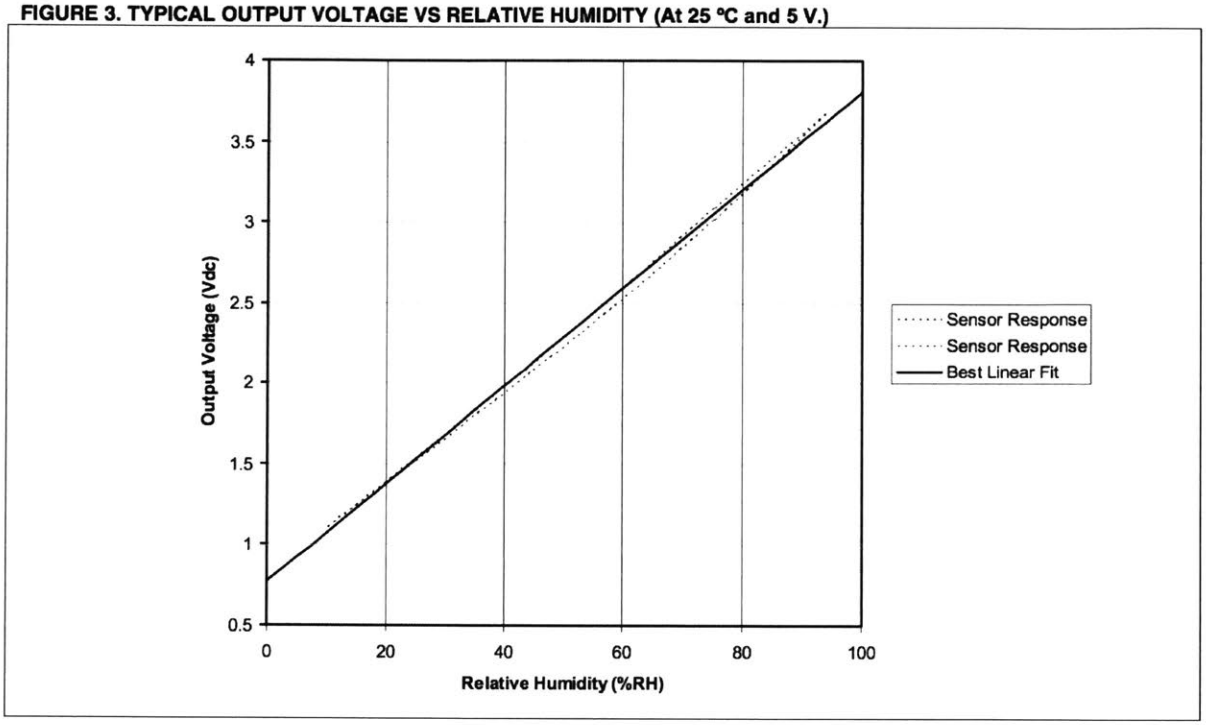

FIGURE 4. TYPICAL OUTPUT VOLTAGE (BFSL) VS RELATIVE HUMIDITY (At 0 °C, 70 °C and 5 V.)

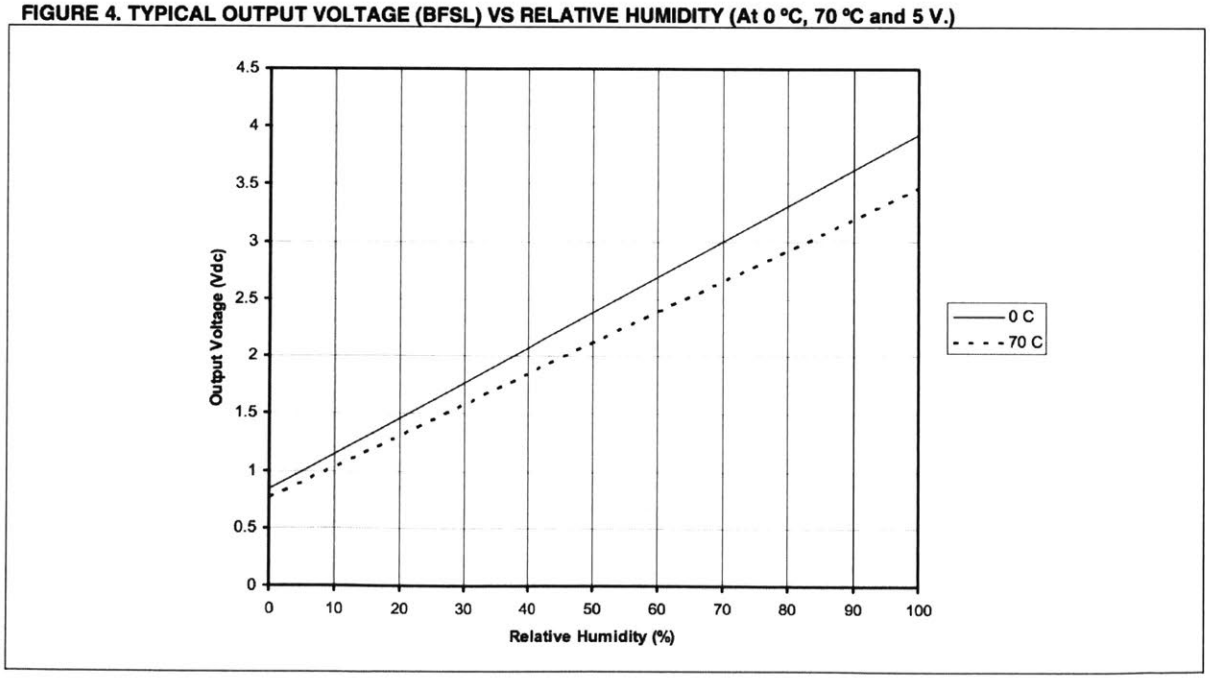

FIGURE 5. HIH-4030 MOUNTING DIMENSIONS (For reference only. mm/[in])

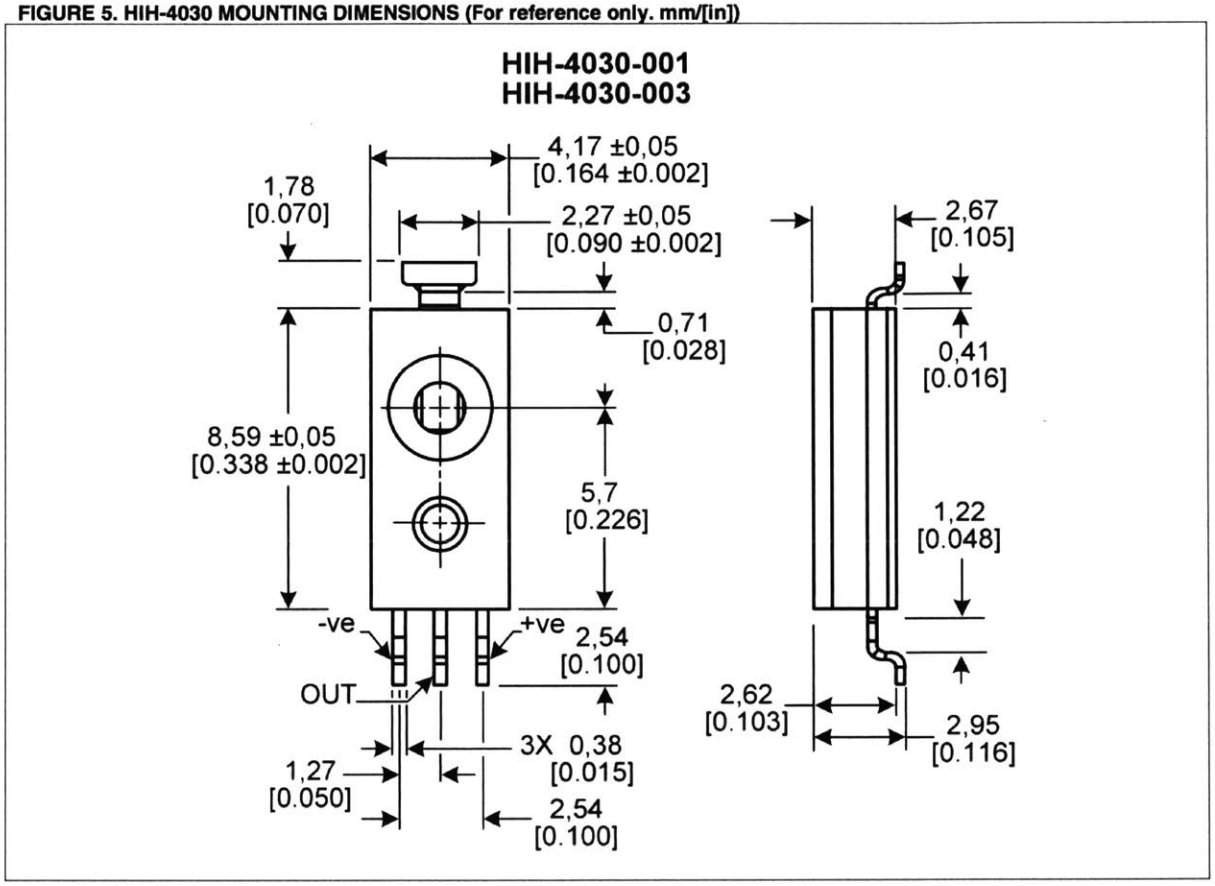

FIGURE 6. HIH-4031 MOUNTING DIMENSIONS (For reference only. mm/[in])

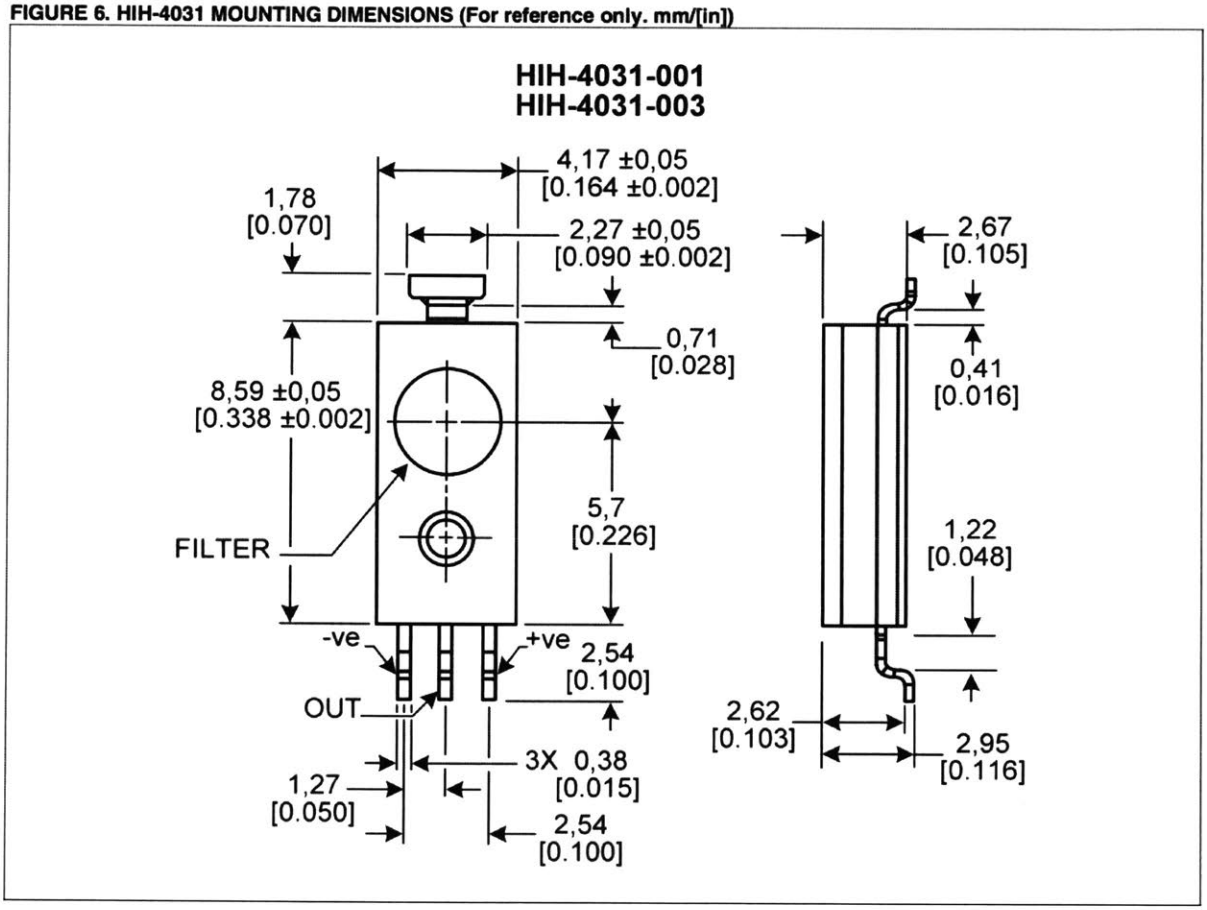

FIGURE 7. HIH-4031 PCB LANDING PATTERN (For reference only. mm/[in])

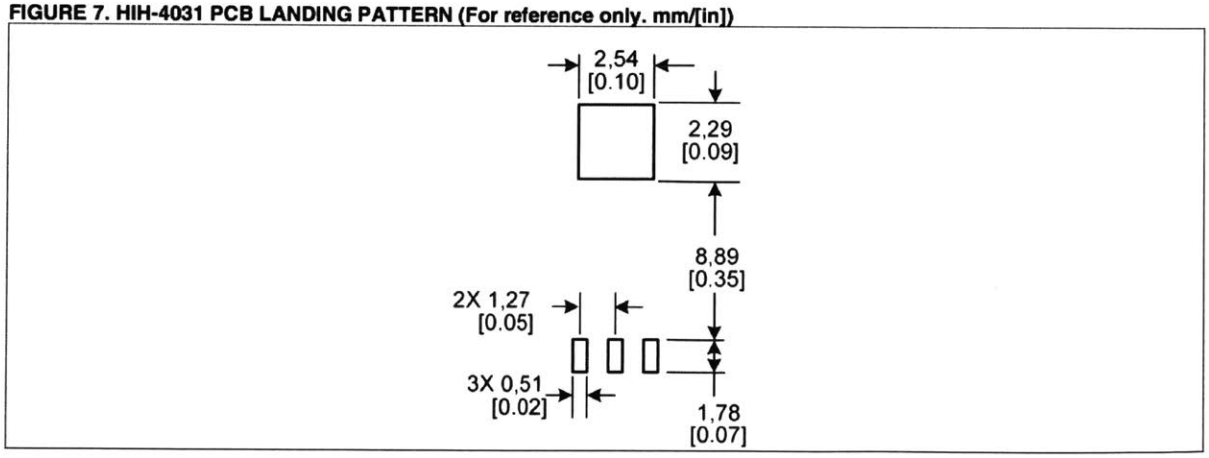

FIGURE 8. TAPE AND REEL DIMENSIONS (For reference only. mm/[in])

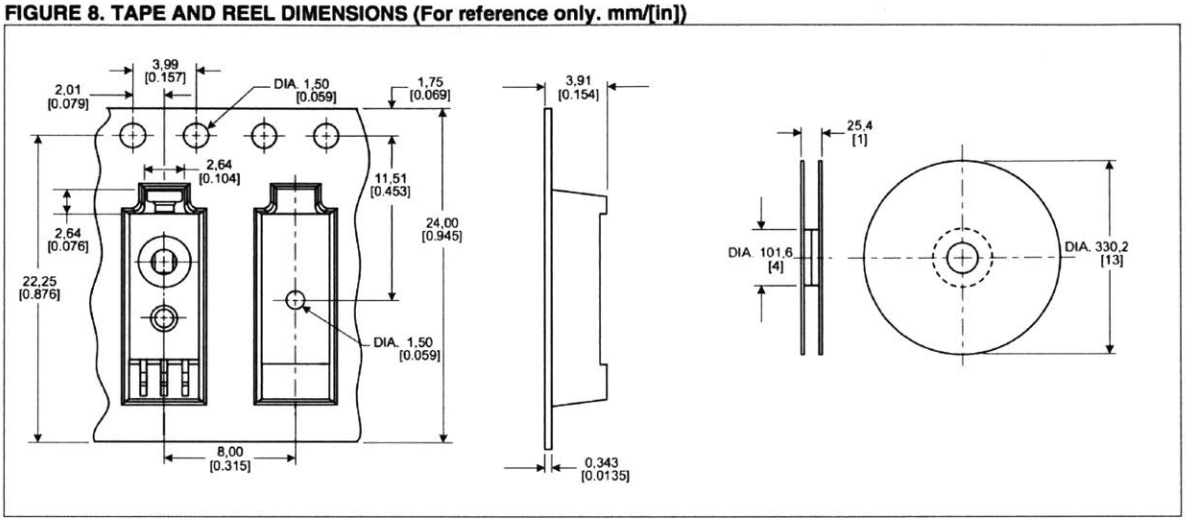

FIGURE 9. TYPICAL APPLICATION CIRCUIT

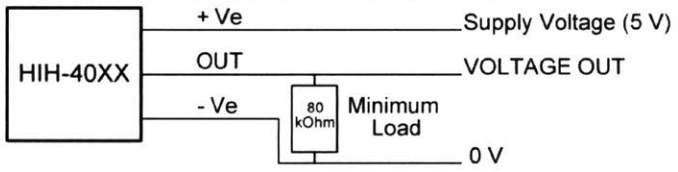

ORDER GUIDE

Catalog Listing	Description
HIH-4030-001	Covered integrated circuit humidity sensor, SMD, 1000 units on tape and reel
HIH-4030-003	Covered integrated circuit humidity sensor, SMD, calibration and data printout, 1000 units on tape and reel
HIH-4031-001	Covered, filtered integrated circuit humidity sensor, SMD, 1000 units on tape and reel
HIH-4031-003	Covered, filtered integrated circuit humidity sensor, SMD, calibration and data printout, 1000 units on tape and reel
HIH-4030-001S	Sample pack: covered integrated circuit humidity sensor, SMD, five units on tape
HIH-4030-003S	Sample pack: covered integrated circuit humidity sensor, SMD, calibration and data printout, five units on tape
HIH-4031-001S	Sample pack: covered, filtered integrated circuit humidity sensor, SMD, sample pack, five units on tape
HIH-4031-003S	Sample pack: covered, filtered integrated circuit humidity sensor, SMD, calibration and data printout, five units on tape

FURTHER HUMIDITY SENSOR INFORMATION

See the following associated literature is available on the Web:

- Product installation instructions
- Application sheets:
  - Humidity Sensor Performance Characteristics
  - Humidity Sensor Theory and Behavior
  - Humidity Sensor Moisture and Psychrometrics
  - Thermoset Polymer-based Capacitive Sensors

GP2Y1010AU0F

Compact Optical Dust Sensor

■ Description

GP2Y1010AU0F is a dust sensor by optical sensing system.
An infrared emitting diode (IRED) and an phototransistor are diagonally arranged into this device.
It detects the reflected light of dust in air.
Especially, it is effective to detect very fine particle like the cigarette smoke.
In addition it can distinguish smoke from house dust by pulse pattern of output voltage.

■ Features

1. Compact, thin package (46.0 × 30.0 × 17.6 mm)
2. Low consumption current (Icc: MAX. 20 mA)
3. The presence of dust can be detected by the photometry of only one pulse
4. Enable to distinguish smoke from house dust
5. Lead-free and RoHS directive compliant

■ Compliance

1. Compliant with RoHS directive (2002/95/EC)

■ Applications

1. Detecting of dust in the air.
2. Example: Air purifier, Air conditioner, Air monitor

Sheet No.: E4-A01501EN
Date Dec. 1. 2006

■ Internal schematic

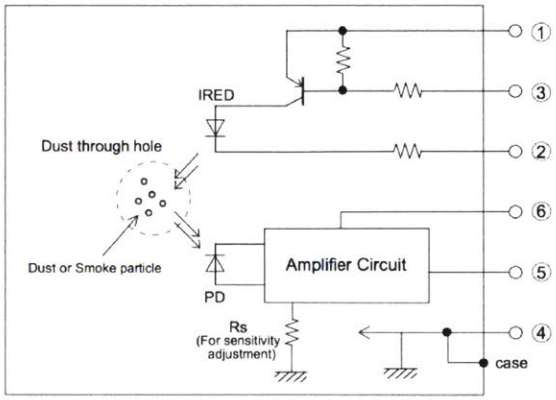

■ Outline Dimensions

(Unit : mm)

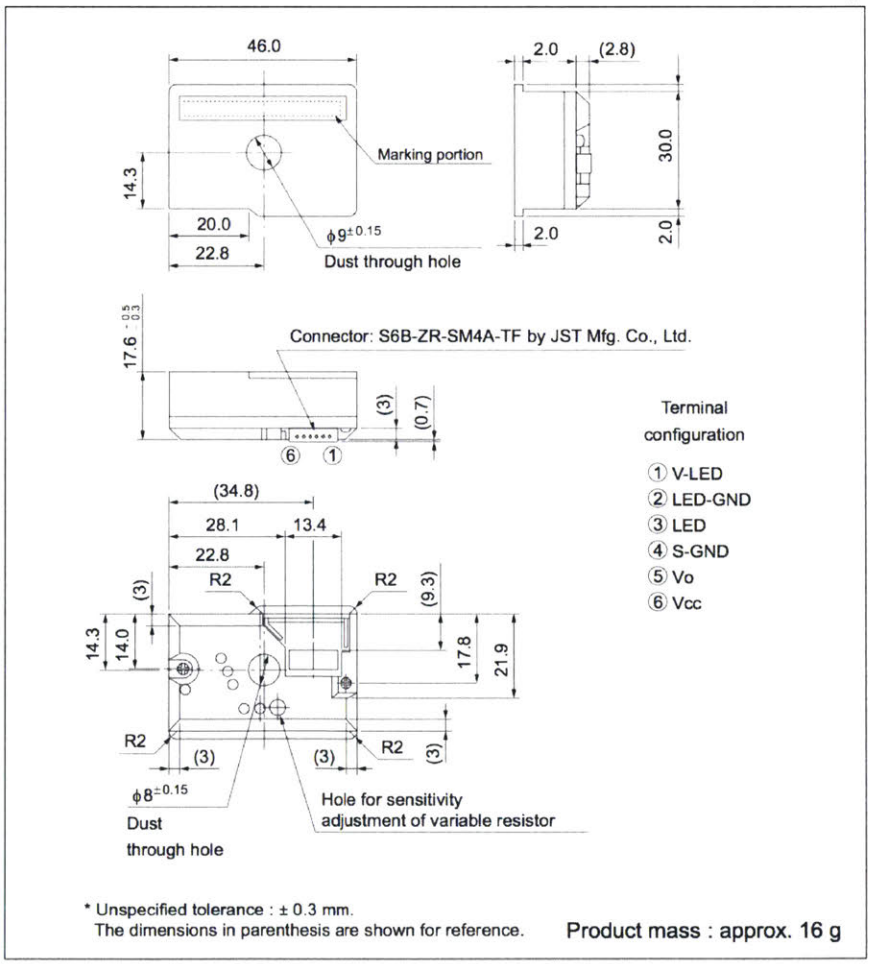

Marking information

Date code (2 digit)

1st digit		2nd digit	
Year of production		Month of production	
A.D.	Mark	Month	Mark
2000	0	1	1
2001	1	2	2
2002	2	3	3
2003	3	4	4
2004	4	5	5
2005	5	6	6
2006	6	7	7
2007	7	8	8
2008	8	9	9
2009	9	10	X
2010	0	11	Y
:	:	12	Z

repeats in a 10 year cycle

Country of origin

Philippines

■ Absolute Maximum Ratings

(T_a=25°C)

Parameter	Symbol	Rating	Unit
Supply voltage	V_{CC}	−0.3 to +7	V
*1 Input terminal voltage	V_{LED}	−0.3 to V_{CC}	V
Operating temperature	T_{opr}	−10 to +65	°C
Soldering temperature	T_{sol}	−20 to +80	°C

*1 Open drain drive input

■ Electro-optical Characteristics

(T_a=25°C, V_{CC}=5V)

Parameter	Symbol	Conditions	MIN.	TYP.	MAX.	Unit
Sensitivity	K	*1 *2 *3	0.35	0.5	0.65	V/(0.1mg/m³)
Output voltage at no dust	V_{OC}	*2 *3	0	0.9	1.5	V
Output voltage range	V_{OH}	*2 *3 R_L=4.7kΩ	3.4	–	–	V
LED terminal current	I_{LED}	*2 LED terminal voltage = 0	–	10	20	mA
Consumption current	I_{CC}	*2 R_L=∞	–	11	20	mA

*1 Sensitivity is specified by the amount of output voltage change when dust density changes by 0.1 mg/m³. And the dust density for detection is a value of the density of cigarette (MILD SEVEN®) smoke measured by the digital dust monitor (P-5L2: manufactured by SHIBATA SCIENTIFIC TECHNOLOGY LTD.).
*2 Input condition is shown in Fig. 1
*3 Output sampling timing is shown in Fig. 2

■ Recommended input condition for LED input terminal

Parameter	Symbol	Value	Unit
Pulse Cycle	T	10 ± 1	ms
Pulse Width	P_W	0.32 ± 0.02	ms
Operating Supply voltage	V_{CC}	5 ± 0.5	V

Fig. 1 Input Condition for LED Input Terminal

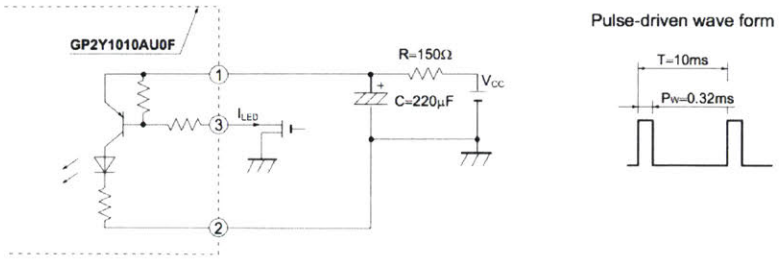

Fig. 2 Sampling Timing of Output Pulse

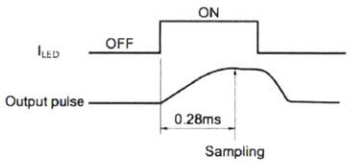

Fig. 3 Output Voltage vs. Dust Density

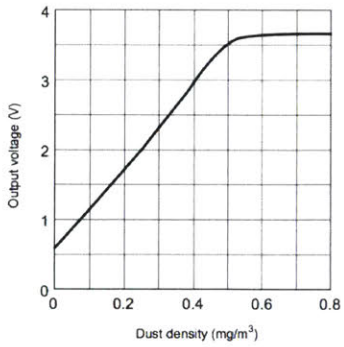

Remarks : Please be aware that all data in the graph are just for reference and are not for guarantee.

• Notes

1 Connection of case and GND
Case material use conductive resin as cover case {printed model No.} and metal {test terminal side} as bottom cover. The metal case connects with GND in sensor.

2 Cleaning
Please don't do cleaning, because there is a case that this device is not satisfied with its characteristics by cleaning.

3 Pulse input range
Please subject to recommendation as regard input condition for LED in order to keep reliability.

4 Dust adhesion
There is a case that this product does not detect the dust density correctly, since the dust adhered to the inside of the dust through hole may project into the detecting space which consist of emitter and detector light axis. Please take the structure and mechanism of the equipment into consideration to avoid the influence of adhered dust. And when the dust is adhered, please consider the maintenance such as vacuuming or blowing off the dust by air.
In addition, please pay attention to structure and placing location of the application to avoid any adhesive particle like oil, etc. to gets into the device. If it sticks to optical part, malfunction may occur.

5 Light output
In circuit designing, make allowance for the degradation of the light emitting diode output that results from long continuous operation. (50% degradation/5 years)

6 Sensitivity adjustment VR
VR for sensitivity adjustment is set up at shipping from sharp. Please do not touch the VR or Electro-optical characteristics specified on the specification will be invalid.

7 Resolution
Please do not disassemble the device such as removing tapping screw and so on. Even if the device is reassembled, it may not satisfy the specification.

8 Application to fire alarm
Please do not use this device for a fire alarm application. When using this device to application other than air purifying and equipment with air purifying function, please inform us before usage.

9 Noise influence
If the sensor is located close to noise generator (ex. Electric dust collector, etc.), the sensor output may be affected by leaded noise. On top of that noise from power supply line also may affect the sensor output. When desinging the system, please consider the effect from noise.

10 Vibration influence
The sensor may change its value under mechanical oscillation. Before usage, please make sure that the device works normally in the application.

11 Incident light influence
There is a case that the sensor output may be affected when outer-light comes through dust through hole on printed side. In order to avoid any influence from outer-light, please locate the printed side of sensor facing to inside of the application.

12 When inside of the sensor is moisturized, this product does not keep its proper function. Please design the application so that moisturization of the sensor does not happen.

Appendix C

MATLAB Code

This appendix documents the two main MATLAB scripts that were written for this study.

C.1 Dust Video Analysis

The following code was written to analyze the dust videos discussed in Chapter 4. This code performs the desired analysis on the video frame data to calculate the change in average pixel intensity caused by an increase in airborne dust concentration. The analysis performed by this code is described in more detail in Chapter 4.

```
% Video Processing Code for Dust Analysis

%import video file
video = VideoReader('Trial1.MOV');

%create baseline image from the first frame of the video, and convert
 to
%grayscale
baseline = readFrame(video);
graybase = rgb2gray(baseline);

%average all the pixel intensity values from this baseline
basemean = mean(mean(graybase));

%initialize matrices to store average pixel intensities for each frame
gmatrix = zeros(1,400);
%initialize an array tracking the frame number
frames = linspace(1,400,400);

ii = 1;

while hasFrame(video)
   %read the current frame
   img = readFrame(video);
   %convert to grayscale
   imggray = rgb2gray(img);
   %calculate average pixel intensity of current frame in grayscale
   gmean = mean(mean(imggray));

   %determine the change in average pixel intensity from baseline
 image to
   %current frame
   gintensity = basemean-gmean;

   %store this value, using ii to record the frame number
   gmatrix(ii) = gintensity;

   %move on to the next frame
   ii = ii+1;
end

%Plot the results
figure(1)
plot(frames,gmatrix);
```

Figure C-1: MATLAB code for dust video processing

C.2 Pendulum Simulation

The following code was written to solve the nonlinear pendulum differential equation. This equation and its derivation are described in detail in Chapter 5.

```
%Pendulum ODE Solver Code - this script solves the differential
 equations
%for pendulum motion

%initialize constants for gravity g, length L, damping b, and mass m
g = 9.80665;
L = .246;
b = .000497;
m = 0.0277217;

%Use ode45 function to solve the differential equations without
 damping
%present, solving for theta and time
[t,theta] = ode45(@(t,theta) pend(t,theta,g,L),[10 30],[0.6199; 0]);

%solve for y using the theta values
y = L.*sin(theta);

%Use ode45 function to solve the differential equations with damping
[td,thetad] = ode45(@(td,thetad) damppend(td,thetad,g,L,b,m),[0 30],
[0.6199; 0]);

%solve for damped y
yd = L.*sin(thetad(:,1));

%calculate the derivative of damped y, to determine the velocity of
 the
%pendulum
dyd = L.*cos(thetad(:,1)).*thetad(:,2);

%plot the results, comparing damped and undamped responses
close all
figure(1);
plot(t,y(:,1),'-o')

hold on
plot(td,yd(:,1),'-')
hold off
```

Figure C-2: MATLAB code to solve pendulum differential equations

```
function dthetadt = pend(t,theta,g,L)

dthetadt = [theta(2); -g/L*sin(theta(1))];

end
```

Figure C-3: MATLAB function for undamped pendulum differential equation

```
function dthetadt = damppend(t,theta,g,L,b,m)

dthetadt = [theta(2); -g/L*sin(theta(1))-b/m*theta(2)];

end
```

Figure C-4: MATLAB function for damped pendulum differential equation

Bibliography

[1] United States Department of Labor. Coal fatalities for 1900 through 2016. Online, 2017.

[2] Xueqiu He and Li Song. Status and future tasks of coal mining safety in China. *Saf. Sci.*, 50(4):894–898, April 2012.

[3] Hong Chen, Qun Feng, Ruyin Long, and Hui Qi. Focusing on coal miners' occupational disease issues: A comparative analysis between China and the United States. *Saf. Sci.*, 51(1):217–222, January 2013.

[4] Center for Disease Control. History of the mining program. Online, Sep 2012.

[5] http://www.dji.com/. Dji official website. Online, 2017.

[6] Nils Gageik, Paul Benz, and Sergio Montenegro. Obstacle detection and collision avoidance for a UAV with complementary low-cost sensors. *IEEE Access*, 3:599–609, 2015.

[7] S. Bouabdallah, M. Becker, V. de Perrot, and R. Siegwart. Toward obstacle avoidance on quadrotors. *Proc. 12th International Symposium on Dynamic Problems of Mechanics*, pages 1–10, 2007.

[8] J. F. Roberts, T. S. Stirling, J. C. Zufferey, and D. Floreano. Quadrotor using minimal sensing for autonomous indoor flight. *Proc. MAV*, pages 1–8, 2007.

[9] Joao Machado Santos, Micael S. Couceiro, David Portugal, and Rui P. Rocha. A sensor fusion layer to cope with reduced visibility in slam. *J. Intell. Robot. Syst.*, 80(3-4):401–422, December 2015.

[10] Jorge Sales, Raul Marin, Enric Cervera, Sergio Rodriguez, and Javier Perez. Multi-sensor person following in low-visibility scenarios. *Sensors*, 10(12):10953–10966, December 2010.

[11] Christopher Brunner, Thierry Peynot, Teresa Vidal-Calleja, and James Underwood. Selective combination of visual and thermal imaging for resilient localization in adverse conditions: Day and night, smoke and fire. *J. Field Robot.*, 30(4):641–666, Jul-Aug 2013.

[12] Abraham Bachrach, Samuel Prentice, Ruijie He, and Nicholas Roy. RANGE-Robust autonomous navigation in GPS-denied environments. *J. Field Robot.*, 28(5):644–666, Sep-Oct 2011.

[13] J. Pascoal, L. Marques, and A. T. de Almeida. Assessment of laser range finders in risky environments. *IEEE International Conference on Intelligent Robots and Systems*, pages 3533–3538, 2008.

[14] V. Tretyakov and T. Linder. Range sensors evaluation under smoky conditions for robotics applications. *IEEE International Symposium on Safety, Security, and Rescue Robotics*, pages 215–220, 2011.

[15] B. Yamauchi. All-weather perception for man-portable robots using ultra-wideband radar. *IEEE International Conference on Robotics and Automation*, July 2010.

[16] I. Gresham, A. Jenkins, R. Egri, C. Eswarappa, N. Kinayman, N. Jain, R. Anderson, F. Kolak, R. Wohlert, S. P. Bawell, J. Bennett, and J. P. Lanteri. Ultra-wideband radar sensors for short-range vehicular applications. *IEEE Trans. Microw. Theory Tech.*, 52(9):2105–2122, September 2004.

[17] R.J. Fontana, E.A. Richley, A.J. Marzullo, L.C. Beard, R.W.T. Mulloy, and E.J. Knight. An ultra-wideband radar for micro air vehicle applications. *IEEE Conference on Ultra Wideband Systems and Technologies*, May 2002.

[18] J. Seitz, M. Schaub, O. Hirsch, R. Zetik, T. Deissler, R. Thoma, and J. Thielecke. UWB feature localization for imaging. *IEEE International Conference on Ultra-Wideband*, 2, 2008.

[19] T. Deissler and J. Thielecke. UWB SLAM with rao-blackwellized monte carlo data association. *International Conference on Indoor Positioning and Indoor Navigation*, 2010.

[20] J. C Toomay and Paul J Hannen. *Radar principles for the non-specialist.* SciTech Pub., Edison, NJ, 3rd ed edition, 2004.

[21] H. Weber. The fresnel equations for lossy dielectrics and conservation of energy. *J. Mod. Opt.*, 61(15):1219–1224, 2014.

[22] M. G. M. Hussain. Ultra-wideband impulse radar - an overview of the principles. *IEEE Aerosp. Electron. Syst. Mag.*, 13(9):9–14, September 1998.

[23] Faranak Nekoogar. *Ultra-wideband communications: fundamentals and applications.* Prentice Hall Professional Technical Reference, Upper Saddle River, NJ, 2006.

[24] C. N. Paulson, J. T. Chang, C. E. Romero, J. Watson, F. J. Pearce, and N. Levin. Ultra-wideband radar methods and techniques of medical sensing and imaging. *SPIE International Symposium on Optics*, Oct 2005.

[25] https://walabot.com/. Walabot official website. Online, 2017.

[26] https://www.xethru.com/x2-uwb-radar chip.html/. Xethru official website. Online, 2017.

[27] J. Feng, X. Kang, Q. Zuo, C. Yuan, W. Wang, Y. Zhao, L. Zhu, H. Lu, and J. Chen. Fabrication and evaluation of a graphene oxide-based capacitive humidity sensor. *Sensors (Basel)*, 16(3):314, Mar 2016.

[28] A. V. Magaldi, M. Mateu, J. Bech, and J. Lorente. A long term (1999-2008) study of radar anomalous propagation conditions in the western mediterranean. *Atmos. Res.*, 169:73–85, March 2016.

[29] Philippe Lopez. A 5-yr 40-km-resolution global climatology of superrefraction for ground-based weather radars. *J. Appl. Meteorol. Climatol.*, 48(1):89–110, January 2009.

[30] Barbara Hughey. MIT 2.671 (Measurement and Instrumentation) Course Notes. Online, Aug 2014.